



HAL
open science

Luminescence and up-conversion properties in $\text{La}_2\text{Ti}_2\text{O}_7:\text{Eu}^{3+},\text{Er}^{3+}$ oxides under UV and NIR radiations towards a two-color sensor

Fabien Szczepanski, Alexandre Bayart, Arturas Katelnikovas, Jean-François Blach, Jolanta Rousseau, Sébastien Saitzek

► To cite this version:

Fabien Szczepanski, Alexandre Bayart, Arturas Katelnikovas, Jean-François Blach, Jolanta Rousseau, et al.. Luminescence and up-conversion properties in $\text{La}_2\text{Ti}_2\text{O}_7:\text{Eu}^{3+},\text{Er}^{3+}$ oxides under UV and NIR radiations towards a two-color sensor. *Journal of Alloys and Compounds*, 2020, 826, pp.154157. 10.1016/j.jallcom.2020.154157 . hal-02567005

HAL Id: hal-02567005

<https://hal.science/hal-02567005>

Submitted on 7 Mar 2022

HAL is a multi-disciplinary open access archive for the deposit and dissemination of scientific research documents, whether they are published or not. The documents may come from teaching and research institutions in France or abroad, or from public or private research centers.

L'archive ouverte pluridisciplinaire **HAL**, est destinée au dépôt et à la diffusion de documents scientifiques de niveau recherche, publiés ou non, émanant des établissements d'enseignement et de recherche français ou étrangers, des laboratoires publics ou privés.



Distributed under a Creative Commons Attribution - NonCommercial 4.0 International License

1 **Luminescence and up-conversion properties in $\text{La}_2\text{Ti}_2\text{O}_7:\text{Eu}^{3+},\text{Er}^{3+}$ oxides**
2 **under UV and NIR radiations towards a two-color sensor**

3
4 Fabien Szczepanski ¹, Alexandre Bayart ¹, Arturas Katelnikovas ², Jean-François Blach ¹,
5 Jolanta Rousseau ¹, Sébastien Saitzek ^{1,*}

6
7 1 Univ. Artois, CNRS, Centrale Lille, ENSCL, Univ. Lille, UMR 8181, Unité de Catalyse et
8 Chimie du Solide (UCCS), F-62300 Lens, France

9 2 Institute of Chemistry, Vilnius University, Naugarduko 24, Vilnius LT-03225, Lithuania
10

11
12
13
14
15
16
17
18
19
20
21
22
23

24 ***Corresponding author:**

25 **Pr. Sébastien SAITZEK,**

26 ¹Université d'Artois, Unité de Catalyse et de Chimie du Solide, UCCS,

27 *Axe Chimie du Solide, CNRS-UMR 8181, Faculté des Sciences Jean Perrin,*

28 *F-62300 LENS, France*

29 Phone: +33 / 321791732, Fax: +33 / 321177955, E-mail: sebastien.saitzek@univ-artois.fr

30

31 Abstract

32

33 $\text{La}_{2-x-y}\text{Eu}_x\text{Er}_y\text{Ti}_2\text{O}_7$ oxides have an emission color which depends on the excitation
34 wavelength. Under the UV excitation (310 to 393 nm), they emit in the red spectral region
35 and, under NIR excitation (785 to 980 nm), they exhibit a green emission induced by
36 upconversion luminescence from Er^{3+} ions. The structural and luminescence properties of
37 these oxides synthesized by the solid state reaction method were studied according to the x
38 and y values. The co-substituted oxides are obtained over a composition zone between $x \leq 0.2$
39 and $y \leq 0.05$. Beyond these values, a phase mixture consisting of a monoclinic phase (layered-
40 perovskite) and cubic phase (pyrochlore) is observed. Under the UV excitation, the reddish
41 emission color is mainly induced by the Eu^{3+} ions via an exchange interaction mechanism.
42 The quenching concentration of Eu^{3+} ions is dependent on the excitation wavelength: $x = 0.3$
43 and 0.6, at 310 and 377 nm, respectively. With the measurements of photoluminescence decay
44 curves, the lifetime kinetics was linked to the Eu^{3+} ions concentration. The CIE 1931 color
45 coordinates were also determined according to the x and y values. This one shows linear
46 evolutions when x is fixed and y is variable and vice versa. The good chemical and thermal
47 stability of these oxides also make it possible to disperse them effectively in a glass of lithium
48 tetraborate. Only a 2% transmittance drop is observed for the insertion of 2% wt. of the oxide.
49 The upconversion luminescence properties were also measured under NIR excitation and
50 shown an emission in the green spectral region mainly due to Er^{3+} ions. The study of emission
51 intensity dependence on the laser power led to the conclusion of a two-photon excitation
52 process. Temperature-dependent upconversion emission follows a Mott-Seitz model. The
53 activation energy for ${}^4\text{F}_{9/2} \rightarrow {}^4\text{I}_{15/2}$ quenching was found to be 52.8 meV.

54

55 1. Introduction

56

57 During the last decades, inorganic or hybrid materials with luminescence properties
58 have been widely studied and are currently used in many devices of our daily life [1],[2].
59 Among these compounds, inorganic materials based on rare earth ions contained in a host-
60 matrixes such as oxides, silicates, aluminates, aluminosilicates, aluminoborates, molybdates,
61 tungstates, etc., are those the most studied by the scientific community [3]. Downconversion
62 (emission in the visible range under a UV light excitation) and upconversion (emission in the
63 visible range under a NIR excitation / absorption of two or more photons) luminescence
64 properties can find many application fields such as fluorescent lamps [4], radiation sensors
65 [5], optical temperature sensors [6], phosphors for LED industry [7], anti-counterfeiting ink
66 [8], incoherent laser light source, display technologies [9], biological labeling [10] and many
67 others [11]. Moreover, **the upconverting materials are widely** used in biological applications
68 [12] because their excitation wavelength locates within the NIR optical window of biological
69 tissues and it can thus reach the maximum penetration [13]. As such, the upconversion
70 materials are used in the photodynamic therapy [14] or the photoactivated drug delivery
71 systems [15].

72 Intrinsically, materials that can emit different colors under different types of excitation
73 (UV or NIR) can be particularly attractive for designing multifunctional sensors, anti-
74 counterfeiting inks, multi-color fluorescence imaging or for the biomedical field. Recently, it
75 has been shown that $\text{La}_2\text{Ti}_2\text{O}_7$ oxides can serve as a host matrix for the design of new
76 phosphors with interesting optical properties. Indeed, $\text{La}_2\text{Ti}_2\text{O}_7:\text{Eu}^{3+}$ oxides show **an intense**
77 red emission under UV excitation with a quantum yield of 42% [16]. In addition, we have
78 shown that $\text{La}_{1.9}\text{Er}_{0.1}\text{Ti}_2\text{O}_7$ oxide exhibits upconversion luminescence if excited over a wide
79 NIR excitation wavelength range from 785 to 980 nm [17]. **In this work, we investigated the**
80 **possibility to synthesize multifunctional oxides, from a $\text{La}_2\text{Ti}_2\text{O}_7$ host-matrix co-substituted**
81 **by $\text{Eu}^{3+}/\text{Er}^{3+}$, which can respond differently according to the excitation wavelength (UV or**

82 NIR). In the literature and to the best of our knowledge, studies on co-substituted or co-doped
83 $\text{La}_2\text{Ti}_2\text{O}_7$ are scarce. The $\text{Yb}^{3+}/\text{Er}^{3+}$ system was studied to improve the upconversion
84 properties [18] and the $\text{Pr}^{3+}/\text{Tb}^{3+}$ system was considered in order to get a control of the
85 emission color [19].

86 $\text{La}_2\text{Ti}_2\text{O}_7$ is a multifunctional oxide already known for these features: i) piezoelectric
87 and ferroelectric properties with high Curie temperature ($T_c \sim 1500^\circ\text{C}$) [20], [21]; ii)
88 photocatalytic properties, especially used as photocatalyst for H_2 production by water splitting
89 [22],[23] or for Volatile Organic Compounds (VOCs) degradation [24], [25]; iii)
90 luminescence properties when doped or co-doped with other lanthanide ions, such as Pr^{3+} ,
91 Sm^{3+} , Eu^{3+} , Er^{3+} , Tb^{3+} [16], [26], [27], [28], [29], [19], [18]; iv) its good resistance to ionizing
92 radiation and its use as an immobilization matrix of radionuclides for the nuclear industry
93 [30]. In the literature, there are several studies that describe techniques for producing
94 $\text{La}_2\text{Ti}_2\text{O}_7$ oxides. Among them, we can mention the solid state reaction, the sol-gel route [31],
95 [32], [33], hydrothermal method [22], floating zone method for single crystals [21] and many
96 others [34], [35], [36]. $\text{La}_2\text{Ti}_2\text{O}_7$ crystallizes in monoclinic/layered perovskite structure with
97 $P2_1$ space group (#4). The unit cell consists of four corner-sharing TiO_6 octahedra separated
98 by two layers of La-site cations along \vec{c} -axis and infinite chains of corner-sharing TiO_6
99 octahedra along \vec{a} - and \vec{b} -axis. The stability of the monoclinic/layered perovskite structure
100 can be affected during the substitution of La-site by another lanthanide. Indeed, the
101 monoclinic structure is conserved for ionic ratio $r(\text{Ln}^{3+})/r(\text{Ti}^{4+})$ higher than 1.78 (i.e., $\text{Ln}^{3+} =$
102 La^{3+} to Nd^{3+}). While for $r(\text{Ln}^{3+})/r(\text{Ti}^{4+})=1.46$ to 1.78 (i.e. $\text{Ln}^{3+}=\text{Sm}^{3+}$ to Lu^{3+}), a
103 cubic/pyrochlore structure with $Fd\bar{3}m$ space group (#227) is favored [37],[38].

104 In this work, we have synthesized a series of co-substituted $\text{La}_{2-x-y}\text{Eu}_x\text{Er}_y\text{Ti}_2\text{O}_7$ oxides
105 in order to determine the stability limit of the monoclinic/layered perovskite structure and

106 **study the luminescence properties** of these oxides under UV and NIR excitation. For that, the
107 classical luminescence and upconversion measurements (excitation and emission spectra,
108 photoluminescence lifetime, quantum efficiency, thermal quenching mechanisms, and
109 CIE 1931 chromaticity coordinates) were performed.

110

111 **2. Experimental Section**

112

113 $\text{La}_{2-x-y}\text{Eu}_x\text{Er}_y\text{Ti}_2\text{O}_7$ oxides were synthesized by a conventional solid state reaction
114 method. The lanthanide oxides (La_2O_3 , Eu_2O_3 and Er_2O_3 – 99.99% Strem Chemicals) and
115 titanium dioxide (TiO_2 – 99.99% Sigma Aldrich) were used as starting materials. **Before the**
116 **synthesis, the lanthanide oxides were annealed at 800 °C for 5 h in order to avoid the**
117 **lanthanum hydroxide formation which could disturb the good stoichiometry of the final**
118 **product.** The precursors weighed in stoichiometric proportions were mixed for 20 min with a
119 few drops of ethanol **and then calcined** at 1100 °C for 12 h under air. The calcination and
120 milling steps were repeated twice to improve the sample homogeneity.

121 **The X-Ray Diffraction (XRD) measurements** were performed using a Rigaku
122 ULTIMA IV diffractometer equipped with Cu anticathode ($\lambda(\text{K}\alpha) = 1.5418 \text{ \AA}$), Soller slits to
123 limit the divergence of X-ray beam, and a nickel foil filter to attenuate the Cu $\text{K}\beta$ line. XRD
124 patterns were recorded in the range of 10° - 90° (scan speed was $0.1^\circ/\text{min}$) using the Bragg-
125 Brentano configuration. The Scanning Electron Microscopy (SEM) images **were recorded**
126 using Hitachi S4700 microscope equipped with **a Field Emission Gun (FEG)**. The optical
127 properties of $\text{La}_2\text{Ti}_2\text{O}_7:\text{Eu}^{3+}$, Er^{3+} oxides were characterized using **a UV-2600**
128 spectrophotometer (Shimadzu). Room-temperature excitation and emission spectra were
129 recorded on **an Edinburgh Instruments FLS980** spectrometer equipped with a double grating

130 Czerny-Turner excitation and emission monochromators. For upconversion experiments, two
131 CW (Continuous Wave) lasers emitting at 808 and 980 nm were employed as the excitation
132 sources. The Thermal Quenching (TQ) measurements were performed using a cryostat
133 “MicrostatN” from the Oxford Instruments coupled to the Edinburgh Instruments FLS980
134 spectrometer. Liquid nitrogen was used as a cooling agent and the measurements were
135 performed at 77 K and at 100–500 K with 50 K steps. The temperature stabilization time was
136 90 s and the temperature tolerance was set to ± 5 K. During the measurements, dried nitrogen
137 was flushed over the cryostat window to avoid the water condensation on the window surface
138 at low temperatures. Finally, the CIE 1931 chromaticity coordinates (Commission
139 Internationale de l’Éclairage – CIE) were calculated from the emission spectra. The color
140 coordinates were calculated in the range of 360-830 nm.

141

142 3. Results and Discussions

143 3.1 Structural and Optical Characterizations

144 The XRD patterns of $\text{La}_{2-x-y}\text{Eu}_x\text{Er}_y\text{Ti}_2\text{O}_7$ powders are presented in Figure 1. According
145 to the substitution percentage, the $\text{La}_2\text{Ti}_2\text{O}_7$ monoclinic structure (ICSD-1950) [39] is
146 maintained when the Eu^{3+} and Er^{3+} contents in the structure are lower than 0.20 and 0.10,
147 respectively. Beyond these substitution values, a phase mixture of a substituted monoclinic
148 phase and cubic/pyrochlore phases such as $\text{Eu}_2\text{Ti}_2\text{O}_7$ (ICSD-83596) [40] and $\text{Er}_2\text{Ti}_2\text{O}_7$ (ICSD-
149 249070) [41], which are indicated by a star in Figure 1, is obtained. We can note that the
150 presence of a low concentration of Er^{3+} (ca. $y=0.05$) greatly limits the maximum substitution
151 rate of Eu^{3+} . This one is limited to $x = 0.20$, whereas, in a previous study [16], it was shown
152 that it could reach 0.60 without Er^{3+} ions. Knowing that, the stability limit of these structures
153 is linked by the value of the $\text{Ti}^{4+}/\text{Ln}^{3+}$ ionic ratio as indicated in the introductory part. The
154 observed structural feature can, therefore, be explained by the ionic radii values of the

155 lanthanides ($\text{La}^{3+}_{\text{VIII}}$ (1.160 Å), $\text{Eu}^{3+}_{\text{VIII}}$ (1.066 Å) and $\text{Er}^{3+}_{\text{VIII}}$ (1.004 Å)) [30]. Indeed, the
156 ionic radius of the Er^{3+} ion is lower than that of the Eu^{3+} ion which itself is lower than that of
157 the La^{3+} ion. Therefore, the average ionic radius weighted by the substitution percentages (as
158 Vegard's law [42]) quickly reaches the stability limit of the monoclinic phase. Thus, in the
159 interval [$x \leq 0.20$; $y \leq 0.10$], a single phase isostructural with $\text{La}_2\text{Ti}_2\text{O}_7$ oxide is observed. The
160 substitution is evidenced by the slight displacement of the (hkl) diffraction peaks towards the
161 wide angle, reflecting a decrease of the unit cell volume. According to x and y values, this
162 displacement is clearly observed for (hkl) reflections with h and k \neq 0 (enlargement shown in
163 Figures 1c and 1d), while the position of the (00l) reflection is not affected. This behavior,
164 already observed for mono-substitution, can be explained by the layered-perovskite structure.
165 Indeed, it is formed by an infinite sequence of TiO_6 octahedra along \vec{a} - and \vec{b} -axes and sheets
166 consisting of four TiO_6 octahedra separated by an Ln-interleaves along the \vec{c} -axis. Thus, the
167 decrease of the ionic radius of the lanthanide ion has a great influence on the infinite chains of
168 octahedra, explaining the evolution of the a and b cell parameters. Consequently, the Ln-
169 interleaves placed between sheets are placed in a less dense layer which can be modified to
170 counterbalance the cationic modification and permits to explain the relative stability of the c
171 cell parameter. In addition, Zhang *et al.* [43] have shown that the $\text{La}_2\text{Ti}_2\text{O}_7$ had a high
172 compressibility along the \vec{c} -axis. This direction is, therefore, less sensitive to the modification
173 of the ionic radius and also makes it possible to explain the stability of the c cell parameter.

174 The morphology of $\text{La}_{2-x-y}\text{Eu}_x\text{Er}_y\text{Ti}_2\text{O}_7$ observed by SEM images are presented in
175 Figure 2. For the low substitution rates (Figure 2a and 2b), aggregates consisting of uniform
176 particles of submicron size are observed with homogenous grain-size distribution. When the
177 substitution rates increase, the grain-size distribution becomes more random (Figure 2c and
178 2d) probably reflecting the multiphasic character observed in the XRD experiments. For
179 substantial substitutions of La by Eu and Er elements (in order to avoid the detection limit),

180 the Energy Dispersive X-Ray (EDX) analyzes confirm also a uniform distribution of La, Ti,
181 Eu and Er elements in the matrix (corresponding to the values expected by the stoichiometric
182 calculations).

183 The optical properties of $\text{La}_{2-x-y}\text{Eu}_x\text{Er}_y\text{Ti}_2\text{O}_7$ phosphors were characterized by UV-
184 visible diffuse reflectance spectra. The absorption spectra were recorded for all samples. In
185 Figure 3, the typical room temperature absorption spectra for $\text{La}_{1.85}\text{Eu}_{0.10}\text{Er}_{0.05}\text{Ti}_2\text{O}_7$, $\text{Eu}_2\text{Ti}_2\text{O}_7$
186 and $\text{Er}_2\text{Ti}_2\text{O}_7$ oxides are shown. Except $\text{Eu}_2\text{Ti}_2\text{O}_7$ sample, each transition assignment in the
187 spectra corresponds to the excited level of Er^{3+} ions starting from the ground state $^4\text{I}_{15/2}$. So,
188 the transitions bands centered at 378, 454, 466, 522, 538, 653 and 798 nm correspond to
189 $^4\text{G}_{11/2}$, $^4\text{F}_{3/2; 5/2}$, $^4\text{F}_{7/2}$, $^2\text{H}_{11/2}$, $^4\text{S}_{3/2}$, $^4\text{F}_{9/2}$ and $^4\text{I}_{9/2}$ of Er^{3+} energy levels, respectively [44]. For
190 $\text{Eu}_2\text{Ti}_2\text{O}_7$ oxide, the intensities of absorption lines, attributable to the excited states of Eu^{3+}
191 ions, are very low. In order to identify them, it is necessary to zoom at the base of peak
192 starting at 350 nm (inset of Figure 3a). The broad and intensive absorption band in the range
193 of 200–340 nm occurs due to $\text{Eu}^{3+}\text{-O}^{2-}$ Charge Transfer (CT) transition. The sets of lines
194 centered at 394, 465, 427 and 589 nm correspond to transitions originating from the $^7\text{F}_{0,1}$
195 ground state of Eu^{3+} ions to $^5\text{L}_6$, $^5\text{D}_2$, $^5\text{D}_1$ and $^5\text{D}_0$ excited states, respectively [45]. $\text{La}_2\text{Ti}_2\text{O}_7$
196 oxide is a semi-conductor material, thus, the optical band-gap (E_g) can be determined by the
197 Tauc plot based on the following equation [42]:

$$198 \quad \alpha h\nu = A(h\nu - E_g)^n \quad (1)$$

199 Here α is the absorption coefficient, $h\nu$ corresponds to the photon energy, A is a
200 proportionality constant and E_g represents the optical band-gap. Finally, the exponent n
201 denotes the nature of the transition. Here, $\text{La}_2\text{Ti}_2\text{O}_7$ compound is known to have a direct
202 allowed transition; thus, the equations were solved with $n = 1/2$ [46]. As illustrated in Figure
203 3b, the $(\alpha h\nu)^2$ vs. $h\nu$ plots, allow to determine the effective optical band-gaps by extrapolating
204 the linear region of the curves to the $h\nu$ axis intercept. We observed that the E_g values are very

205 close and decrease slowly with the decrease of the Ln^{3+} ionic radius. The E_g values are 3.85,
206 3.78 and 3.77 eV for $\text{La}_{1.85}\text{Eu}_{0.10}\text{Er}_{0.05}\text{Ti}_2\text{O}_7$, $\text{Eu}_2\text{Ti}_2\text{O}_7$ and $\text{Er}_2\text{Ti}_2\text{O}_7$, respectively.

207 3.2 Luminescence properties

208 The room-temperature (RT) excitation and emission spectra recorded in the range from 250 to
209 800 nm for a $\text{La}_{1.6}\text{Eu}_{0.10}\text{Er}_{0.30}\text{Ti}_2\text{O}_7$ compound are shown in Figure 4. The spectra presented
210 are typical of those recorded on the complete range of $\text{La}_{2-x-y}\text{Eu}_x\text{Er}_y\text{Ti}_2\text{O}_7$ oxides whose
211 evolution in normalized intensity is showed in supplementary materials (Figure S1). First, in
212 the excitation spectrum, two overlapped broad bands are observed around 280 and 310 nm,
213 which can be attributed to the host-related absorption due to the Inter Valence Charge
214 Transfer (IVCT) and the charge transfer (CT) of $\text{Eu}^{3+}/\text{Er}^{3+}-\text{O}^{2-}$, respectively [19] (in
215 correlation with the previous optical band-gap measurements). Depending on the emission
216 wavelength, two different behaviors with many transition bands are observed. These
217 transitions, corresponding to the intra-configurational f-f transitions of Eu^{3+} and Er^{3+} ions, can
218 be indexed using the Dieke diagram [47]. For $\lambda_{\text{em}} = 612.5$ nm, the transitions observed are
219 mostly due to the excited levels of Eu^{3+} ions (i.e., ${}^7\text{F}_0 \rightarrow {}^5\text{D}_4$ (361 nm), ${}^7\text{F}_0 \rightarrow {}^5\text{L}_{7,8}$; ${}^5\text{G}_J$ (375
220 nm), ${}^7\text{F}_0 \rightarrow {}^5\text{L}_6$ (396 nm), ${}^7\text{F}_1 \rightarrow {}^5\text{D}_3$ (412 nm) and ${}^7\text{F}_0 \rightarrow {}^5\text{D}_2$ (465 nm)), while for
221 $\lambda_{\text{em}} = 547.5$ nm the transitions originating from Er^{3+} ions are also rather highlighted (i.e., by
222 ${}^4\text{I}_{15/2} \rightarrow {}^4\text{G}_{7/2}$ (355 nm), ${}^4\text{I}_{15/2} \rightarrow {}^2\text{K}_{15/2}$; ${}^4\text{G}_{9/2}$ (364 nm), ${}^4\text{I}_{15/2} \rightarrow {}^4\text{G}_{11/2}$ (377 nm), ${}^4\text{I}_{15/2} \rightarrow {}^2\text{H}_{9/2}$
223 (406 nm)). In the same way, the emission spectra differ according to the excitation
224 wavelength. Under $\lambda_{\text{exc}} = 310$ nm, many transitions with the most intense line centered at
225 612.5 nm (orange-red spectral range) are observed. These lines can be assigned to Eu^{3+}
226 transitions between the lowest excited ${}^5\text{D}_0$ levels and ${}^7\text{F}_J$ ($J = 0 - 5$) ground state [48], [49],
227 [50]. The splitting of spectral lines is undoubtedly due to a modification of the electronic
228 states by a Stark effect [51]. Under $\lambda_{\text{exc}} = 377$ nm, two green emission bands centered at 525

229 and 548 nm are observed. These bands correspond to the $^2H_{11/2} \rightarrow ^4I_{15/2}$ and $^4S_{3/2} \rightarrow ^4I_{15/2}$
230 transitions of Er^{3+} ions, respectively [52]. In addition, at $\lambda_{exc} = 377$ nm, the ratio between
231 emissions in the green and red ranges varies greatly depending on the x and y values within
232 the $La_{2-x-y}Eu_xEr_yTi_2O_7$ oxides. Thus, a shift of the emission towards the green spectral domain
233 is observed only for Er^{3+} concentrations greater than $y = 0.10$ and for very low concentrations
234 of Eu^{3+} ($x \leq 0.10$), as highlighted on the Figure S1 (Supplementary Material). Beyond this x
235 value, the emission is mainly in the orange-red spectral range. The emission is, therefore,
236 mainly dominated by the effect of Eu^{3+} ions within $La_2Ti_2O_7$ host matrix. Further, under
237 $\lambda_{exc} = 310$ nm, only orange-red emission is observed regardless the x and y values.

238 In Figure 5a, a photograph displaying the emission color of $La_{2-x-y}Eu_xEr_yTi_2O_7$ oxides under
239 the excitation of commercial UV excitation lamp (365 nm) is presented. One can note a
240 difference in intensity that is visible to the naked eye according to the values of x and y. In
241 order to quantify this evolution in the luminescence intensity, we plotted the intensity
242 variations of several emission bands under several excitation wavelengths as a function of the
243 x and y values. The intensity evolution of the $^4S_{3/2} \rightarrow ^4I_{15/2}$ transition at three excitation
244 wavelengths (i.e., 310, 377 and 393 nm) is presented in Figure 5b. The first result indicates
245 that this transition is active only for an excitation wavelength of 377 nm and that its intensity
246 increases progressively with the Er^{3+} ions concentration. The excitation at other mentioned
247 wavelengths resulted in weak to no emission of Er^{3+} ions. This also indicates that the emission
248 due to Eu^{3+} ions dominates mainly under the UV excitation. The intensity evolution of $^5D_0 \rightarrow$
249 7F_2 (the most intense) and $^5D_0 \rightarrow ^7F_4$ transitions under the 310 and 377 nm excitation is
250 presented in Figure 5c in order to highlight the x influence and in Figure 5d to highlight the y
251 influence. In the case of $La_{1.95-x}Eu_xEr_{0.05}Ti_2O_7$ oxides, the intensity of the transitions observed
252 goes through a maximum which is different according to the excitation. These are $x = 0.30$
253 and $x = 0.60$ for 310 and 377 nm, respectively. This difference in the quenching concentration

254 can be explained by an energy transfer between the Er^{3+} and Eu^{3+} ions. Under the excitation at
 255 310 nm, only the Eu^{3+} ions act as activators while under an excitation at 377 nm, the Eu^{3+} and
 256 Er^{3+} ions are both activators. Therefore, under an excitation at 377 nm, **the concentration**
 257 **quenching appears later than it in the case of a mono-substituted oxide.** In a previous study
 258 [16], we showed that for mono-substitution with Eu^{3+} , the quenching concentration is reached
 259 for $x = 0.8$, **that is close to the value determined here. In the case of the oxide $\text{La}_{1.90-}$**
 260 **$y\text{Eu}_{0.10}\text{Er}_y\text{Ti}_2\text{O}_7$, the intensity values of the ${}^5\text{D}_0 \rightarrow {}^7\text{F}_2$ and ${}^5\text{D}_0 \rightarrow {}^7\text{F}_4$ transitions decrease**
 261 **when the y value increases.** Note that for $\lambda_{\text{exc}} = 377$ nm, the relative intensity is significantly
 262 lower than that observed **for the 310 nm excitation.** This also confirms that there is an energy
 263 transfer between the Er^{3+} and Eu^{3+} ions at this wavelength.

264 In addition, we can estimate the critical distance (R_c) by the following formula given by
 265 Blasse [53]:

$$266 \quad R_c = 2 \left(\frac{3V}{4\pi x_c N} \right)^{1/3} \quad (2)$$

267 Here V is the unit cell volume, x_c represents the concentration of activator ions where the
 268 quenching occurs and N is the number of ions whose sites are partially occupied by the
 269 activator in the unit cell (in our case $N = 8$). At $\lambda_{\text{exc}} = 310$ nm and $\lambda_{\text{exc}} = 377$ nm, x_c is equal to
 270 0.175 and 0.325, respectively (sum of Eu^{3+} and Er^{3+} concentration in the oxide). So, **the**
 271 **critical transfer distances are about 3.81 and 4.80 Å, respectively. Knowing that the exchange**
 272 **interaction takes place when the critical distance value is about 3 – 4 Å [54], we can conclude**
 273 **that this mechanism is more accentuated under the excitation at 310 nm.**

274 The room temperature photoluminescence decay curves of $\text{La}_{1.95-x}\text{Eu}_x\text{Er}_{0.05}\text{Ti}_2\text{O}_7$
 275 phosphors are shown in Figure 6a. The samples were excited at 393 nm and the emission was

276 monitored at 612.5 nm ($^5D_0 \rightarrow ^7F_2$ transition). These decay curves can be fitted successfully
277 based on the following multifold exponential equation [55]:

$$278 \quad I(t) = I_0 \sum_i^N A_i e^{-\frac{t}{\tau_i}} \quad (3)$$

279 where, I and I_0 correspond to the luminescence intensity at a given time t and initial
280 intensity, respectively. A_i are pre-exponential constants which are related with the initial
281 intensity, τ_i are the lifetimes for the each exponential components. The average fluorescence
282 lifetime τ_{ave} can be calculated by the following equation [56]:

$$283 \quad \tau_{ave} = \frac{\sum_i^N A_i \tau_i^2}{\sum_i^N A_i \tau_i} \quad (4)$$

284 In our case, the PL decay curves can be fitted with a double exponential function. We can
285 observe a progressive decrease in average life time values with the Eu^{3+} concentration
286 increase. This evolution can be explained by resonant energy transfer between Eu^{3+} ions (and
287 Er^{3+} ions), what leads to decrease of excited state lifetime.

288 We can also note that this double-exponential modeling reveals the different
289 environments for Eu^{3+} cations, as explained by the presence of several crystallographic sites
290 in the monoclinic structure.

291 In addition, Khalil *et al.* [58] have proposed the following equation to describe thermal
292 and concentration quenching [58]:

$$293 \quad \frac{1}{\tau} = K_t = K_r + K_{nr}(T) + K_c [Eu^{3+}] \quad (5)$$

294 Where K_t is the observed decay rate, K_r and $K_{nr}(T)$ are the radiative and non-radiative decay
295 rates, respectively, and K_c is the quenching term dependent on the concentration of europium
296 ions. $K_{nr}(T)$ is dependent on the environment and temperature. This equation can be
297 transposed to our case by adding a component related to the Er^{3+} concentration:

298
$$\frac{1}{\tau} = K_t = K_r + K_{nr}(T) + K_c [Eu^{3+}] + K'_c [Er^{3+}] \quad (6)$$

299 If we consider that the measurements are carried out at a constant temperature and that the
 300 concentration of Er^{3+} ions is constant in samples series, the PL lifetime (or average lifetime) is
 301 directly related to the concentration of Eu^{3+} ions according to the equation:

302
$$\tau_{ave} = \frac{1}{A + K_c [Eu^{3+}]} \quad (7)$$

303 Where A is a constant. **The evolution of an average lifetime as a function of the x is shown in**
 304 **Figure 6b.** We find a decay that can satisfy the expression (7) followed by a bearing from $x =$
 305 0.6. This limit is in good relation with the concentration quenching observed under the 377
 306 nm excitation (see Figure 5c). The average lifetime changes from 894 to 674 μs and K_c can be
 307 calculated by modeling the first part of the curve (dashed line in Figure 6b). This one is worth
 308 $1.299 \times 10^{-3} \mu s^{-1} \cdot at. \%^{-1}$. In the same way, the room temperature PL decay curves of
 309 $La_{1.95-y}Eu_{0.10}Er_yTi_2O_7$ monitored at 393 nm and correspondent to the ${}^5D_0 \rightarrow {}^7F_2$ transition
 310 were also acquired. These curves are shown in Figure S2. The τ_{ave} variation of the lifetime as
 311 a function of y shows a sudden decrease until $y = 0.10$, then an increase. This evolution can
 312 be related to the structural modification experienced by the sample series (see Figure 1).
 313 Indeed, below $y = 0.1$, only **the monoclinic** phase is present and, beyond, a phase mixture is
 314 obtained (monoclinic and cubic). In order to study the Er^{3+} influence, we also recorded the PL
 315 decay curves as a function of x and y for the ${}^4S_{3/2} \rightarrow {}^4I_{15/2}$ transition (Er^{3+}) excited at 377 nm.
 316 **The dependences are shown in Figure S3. Besides the fact that these average PL lifetime**
 317 **values are significantly smaller, if compared to those of the ${}^5D_0 \rightarrow {}^7F_2$ transition of the Eu^{3+}**
 318 **ions, the changes in average PL lifetime values show a sharp fall for low values of x and y .**
 319 This also tells us that the constant K'_c is much higher than the constant K_c . All these results
 320 show a dominance of Eu^{3+} ions on the spectral emission of $La_{2-x-y}Eu_xEr_yTi_2O_7$ oxides.

321 As observed in the photographs of Figure 5a, the $\text{La}_{2-x-y}\text{Eu}_x\text{Er}_y\text{Ti}_2\text{O}_7$ oxides present
322 an intense emission with orange-reddish color. The CIE 1931 chromaticity coordinates have
323 been calculated for the entire series under $\lambda_{\text{exc}} = 310$ nm. In Figure 7a, the 3D plot of CIE
324 1931 coordinates as a function of the atomic percent of europium ions are shown. On the 2D
325 plot projection, we observe a linear variation between the X and Y coordinates (Figure 7b)
326 which illustrates a change of color from orange to red. This color shift can be explained by an
327 intensity increase of the line coming from the $^5\text{D}_0 \rightarrow ^7\text{F}_2$ transition with respect to those of
328 other transitions. In the similar way, the 3D plot of CIE 1931 chromaticity coordinates as a
329 function of the atomic percent of erbium ions are presented in Figure 7c. On the 2D plot
330 projection (Figure 7d), we observe also a linear variation between the X and Y coordinates.
331 This time, we observe a shift from red to orange with the increase in the proportion of erbium.
332 This behavior is explained by a larger intensity decrease for the $^5\text{D}_0 \rightarrow ^7\text{F}_2$ line if compared to
333 that of the $^5\text{D}_0 \rightarrow ^7\text{F}_1$ line. It is known that the $^5\text{D}_0 \rightarrow ^7\text{F}_2$ transition is hypersensitive to the
334 local environment and the $^5\text{D}_0 \rightarrow ^7\text{F}_1$ is insensitive to site symmetry [48]. Consequently, the
335 ratio between these emission intensities defined by $R = I(^5\text{D}_0 \rightarrow ^7\text{F}_2)/I(^5\text{D}_0 \rightarrow ^7\text{F}_1)$, can be
336 used as a sensitive optical probe to determine the symmetry site where Eu^{3+} ion is located
337 [59]. The evolution of the R value is presented in Figure S4 in supplementary materials. We
338 observe a linear decrease of this value between $x = 0.01$ and $x = 0.1$ values of Er^{3+} content in
339 synthesized compounds. This can be explained by a lower distortion of the Eu^{3+} ion
340 occupancy sites due to the insertion of Er^{3+} ions within the layered perovskite structure.
341 Indeed, the Er^{3+} ion radius is smaller, it counterbalances the distortion of the sites of
342 occupation in the monoclinic/layered-perovskite structure. Above $x = 0.1$, a break is observed
343 which may be related to the presence of a phase mixture (monoclinic/cubic), as described in
344 the XRD part. In this case, the cubic phase has centro-symmetric lattice sites that can be
345 occupied by Eu^{3+} ions and, therefore, this also contributes to the decrease of the R ratio.

346 The good thermal resistance and the submicron size of these oxides can allow a homogeneous
347 dispersion in a vitreous matrix to create luminescent glasses for displays, artworks and even
348 anti-counterfeiting markers in luxury flasks. In order to verify this, we carried out a 2% mass
349 dispersion of oxide in a lithium tetraborate matrix. The glass wafer (\varnothing 4 cm, thickness 3 mm)
350 is then formed through the fused bead method. As shown in Figure 8, the transmittance of the
351 glass is very slightly affected by the presence of the oxide. The transmittance drop by 2% is
352 observed in the visible range. Photography under natural light, as shown in inset of Figure 8,
353 highlights the good conservation of **the glass transparency**. Under UV light (365 nm), **the**
354 luminescence is clearly observed with the naked eye (the intensity increases with the
355 concentration of europium, as observed in the case of oxides). The transmission spectrum also
356 shows characteristic transitions of the Er^{3+} and Eu^{3+} ions, which are directly annotated in
357 Figure 8. The absorption lines, observed in transmission spectrum of the glass sample, are just
358 overlapping, as observed in excitation spectra. The good chemical and thermal resistance of
359 these oxides allows us to use them as active material within vitreous matrix.

360

361 **3.3 Up-conversion luminescence properties**

362 The upconversion properties of $\text{La}_{2-x-y}\text{Eu}_x\text{Er}_y\text{Ti}_2\text{O}_7$ oxides were also investigated using
363 two lasers emitting at 808 and 980 nm. In Figure 9a, the emission of the different powders
364 under a laser excitation of 785 nm (power 40 mW) is shown. All samples showed green
365 luminescence visible by naked eye. It is also evident that brightness of emitted light decreases
366 with increasing Eu^{3+} concentration for a fixed Er^{3+} concentration. **The opposite, however, is**
367 **observed if Er^{3+} concentration is increased for the fixed Eu^{3+} content**. This clearly indicate,
368 that high Eu^{3+} concentration quenches upconversion emission of Er^{3+} ions in La_{2-x-}
369 $y\text{Eu}_x\text{Er}_y\text{Ti}_2\text{O}_7$ oxides. The samples with $x = 0.05$, $y = 0.10$ and $x = 0.10$, $y = 0.10$ showed the
370 most intensive upconversion luminescence.

371 The room temperature emission spectra recorded on the $\text{La}_{1.70}\text{Eu}_{0.20}\text{Er}_{0.10}\text{Ti}_2\text{O}_7$ oxide
372 under the excitation at 980 and 808 nm show three main sets of lines attributable to energy
373 levels of the Er^{3+} ion. The bands centered at 520, 547 and 665 nm correspond to
374 ${}^2\text{H}_{11/2} \rightarrow {}^4\text{I}_{15/2}$, ${}^4\text{S}_{3/2} \rightarrow {}^4\text{I}_{15/2}$ and ${}^4\text{F}_{9/2} \rightarrow {}^4\text{I}_{15/2}$ transitions, respectively (Figure 9b). As the
375 conventional luminescence, the multitude of peaks observed is certainly due to a modification
376 of the electronic states by the Stark effect [51]. The mechanism of absorption in upconversion
377 luminescence can follow three main processes [60], [61]: Excited-State Absorption (ESA),
378 Energy Transfer (ET) and Photon Avalanche (PA). The upconversion mechanisms can be
379 evaluated by measuring the upconversion intensity as a function of the laser power. The
380 number of photons (α) which are required to populate the upper emitting level can be
381 obtained by the following relation [62]:

$$382 \quad I \propto P^\alpha \quad (8)$$

383 In order to highlight the process involved, we recorded the emission spectra for
384 different laser powers at 980 nm (Figure 9c). Then, we plotted the evolution $\text{Ln}(I)$ vs. $\text{Ln}(P)$
385 (see Figure 9d). The slope of this curve indicates the number of photons involved in the
386 absorption process. No inflection point is highlighted, therefore, we can exclude an avalanche
387 process of photons. In our case **under the excitation at 980 nm**, we observe linear evolutions
388 whose slopes are 1.23 and 1.50 for the ${}^4\text{S}_{3/2} \rightarrow {}^4\text{I}_{15/2}$ and ${}^4\text{F}_{9/2} \rightarrow {}^4\text{I}_{15/2}$ transitions, respectively.
389 We can suggest that two photons are required to create these mechanisms. This process has
390 already been demonstrated in a previous study on a monosubstitution of $\text{La}_2\text{Ti}_2\text{O}_7$ with Er^{3+}
391 ions [17].

392 The time-resolved measurements performed for ${}^4\text{F}_{9/2} \rightarrow {}^4\text{I}_{15/2}$ transitions under the 980
393 and 808 nm laser excitation are presented in Figure 10, and this reveals that the main
394 excitation mechanism for Er^{3+} ions is excited state absorption regardless the excitation

395 wavelength. The decay curve can be fitted using the sum of two exponential functions, as
 396 described above. Concerning the ${}^4F_{9/2} \rightarrow {}^4I_{15/2}$ transition for the 980 nm laser excitation, we
 397 obtained an average PL lifetime value of 61.6 μs , and, concerning the same transition for the
 398 808 nm laser excitation, the average PL lifetime value of 32.3 μs is obtained. It is evident that
 399 Er^{3+} emission quenches almost twice faster if samples are excited with the 808 nm laser.
 400 Therefore, it can be concluded that the internal efficiency of Er^{3+} is higher for the 980 nm
 401 laser excitation.

402 To complete this study, the temperature-dependent upconversion emission spectra of
 403 $\text{La}_{1.75}\text{Eu}_{0.20}\text{Er}_{0.05}\text{Ti}_2\text{O}_7$ specimen were recorded under the laser excitation at 980 nm and they
 404 are shown in Figure 11a. The conventional emission spectra with the emission bands
 405 attributable to ${}^2H_{11/2} \rightarrow {}^4I_{15/2}$, ${}^4S_{3/2} \rightarrow {}^4I_{15/2}$, ${}^4F_{9/2} \rightarrow {}^4I_{15/2}$ and ${}^4I_{9/2} \rightarrow {}^4I_{15/2}$ transitions, located
 406 at 520, 544, 660 and 811 nm, respectively, are observed. For all transitions, we can see a
 407 gradual decrease in intensity as a function of temperature over a range of 77 to 500 K. This
 408 decrease is induced by thermal quenching effect. This luminescence quenching is due to the
 409 increased probability of non-radiative transitions from excited state to ground state at elevated
 410 temperatures [63]. The temperature dependence of the luminescence can be described by the
 411 Mott-Seitz equation (E_a represents the activation energy for the thermal quenching) [64], [65]:

$$412 \quad I(T) = \frac{I_0}{1 + Ce^{-\frac{E_a}{k_B T}}} \quad (9)$$

413 Where, I_0 and $I(T)$ are the initial intensity and the intensity at the given temperature,
 414 respectively. C is constant, k_B is Boltzmann's constant (8.617×10^{-5} eV/K) and E_a is the thermal
 415 activation energy for the non-radiative transition. Note that, in this expression of the
 416 luminescence decay, the contribution of the phonon-assisted transitions is neglected. The
 417 activation energy can be calculated from a plotting of $\ln[(I_0/I)-1]$ against $1/k_B T$, where a slope
 418 is equal to $-E_a$. The activation energy for ${}^4F_{9/2} \rightarrow {}^4I_{15/2}$ transition quenching was found to be

419 52.8 meV as shown in the inset of Figure 11b. There are several mechanisms that can describe
 420 this thermal quenching phenomenon. The most common is based on energy level diagram
 421 evolving with the temperature. At low temperature, the excited levels are populated and their
 422 de-excitation leads essentially to the emission of luminescence. At high temperature, the
 423 phonon frequency increases leading to increased probability of multi-phonon relaxation and
 424 thus, non-radiative de-excitation of excited states.

425 By normalizing the emitted intensity at 544 nm, we clearly observe an evolution of the
 426 intensities corresponding to the ${}^2\text{H}_{11/2} \rightarrow {}^4\text{I}_{15/2}$ (I_H) and ${}^4\text{S}_{3/2} \rightarrow {}^4\text{I}_{15/2}$ (I_S) transitions with
 427 temperature (Figure S5a in supplementary material). Therefore, the Fluorescence Intensity
 428 Ratio ($FIR(T)=I_H/I_S$) can be employed in thermal sensing [66]. Indeed, the ${}^2\text{H}_{11/2}$ and ${}^4\text{S}_{3/2}$
 429 levels are in thermal equilibrium and the electrons in them obey Boltzmann distribution law;
 430 therefore, $FIR(T)$ can be expressed by the following equation [67]:

$$431 \quad FIR(T) = \frac{I_H}{I_S} = A \exp\left(\frac{-\Delta E}{k_B T}\right) \quad (10)$$

432 Where A is a pre-exponential constant, ΔE is the energy gap separating the ${}^2\text{H}_{11/2}$ and ${}^4\text{S}_{3/2}$
 433 levels, k_B is the Boltzmann constant, and T is the absolute temperature. The calculated values
 434 of I_H/I_S as a function of temperature for $\text{La}_{1.75}\text{Er}_{0.05}\text{Eu}_{0.20}\text{Ti}_2\text{O}_7$ sample are shown in
 435 supplementary material (Figure S5b). The fit of experimentally obtained data with this
 436 previous equation yielded $\Delta E = 565 \pm 28 \text{ cm}^{-1}$ and $A = 4.539 \pm 0.8$. From there, the sensitivity
 437 (S) that defines the change rate of $R(T)$ per unit temperature, can be determined with
 438 following equation [68]:

$$439 \quad S(T) = \frac{dFIR(T)}{dT} = A \exp\left(\frac{-\Delta E}{k_B T}\right) \left(\frac{\Delta E}{k_B T^2}\right) \quad (11)$$

440

441 Since the values of A and ΔE were already obtained, it was possible to model the
442 sensitivity curve. So, as shown in supplementary materials (Figure S5c), the sensitivity
443 reaches maximum of $3.1 \times 10^{-3} \text{ K}^{-1}$ at 405 K and the optimal temperature range of use is
444 defined where the sensitivity S is higher than half of its maximum value S_{Max} as illustrated in
445 Figure S5c in supplementary materials. In a previous study based on $\text{La}_{1.9}\text{Er}_{0.1}\text{Ti}_2\text{O}_7$ oxides
446 (mono-substitution with Er^{3+}), the sensitivity was determined at $1.1 \times 10^{-2} \text{ K}^{-1}$ at 512 K and the
447 useful temperature range was estimated between 250 and 1373 K [17]. To conclude, these
448 oxides can be used for applications of thermal sensing; but in the case of a co-substitution
449 ($\text{Eu}^{3+}/\text{Er}^{3+}$), the Eu^{3+} ions have a detrimental effect with a reduction of the sensitivity (by a
450 ~ 3.7 factor for $\text{La}_{1.75}\text{Eu}_{0.20}\text{Er}_{0.05}\text{Ti}_2\text{O}_7$ oxides) and a reduction in the useful temperature range.
451 This behavior can be explained by non-radiative energy transfer (ET) between energy levels
452 of Er^{3+} and Eu^{3+} ions.

453

454 4. Conclusion

455 The $\text{La}_{2-x-y}\text{Eu}_x\text{Er}_y\text{Ti}_2\text{O}_7$ oxides were successfully synthesized using solid-state
456 reaction. These materials were characterized by X-ray Diffraction, Scanning electron
457 microscopy and fluorescence spectroscopies. We have demonstrated that the monoclinic
458 structure is preserved if Eu^{3+} and Er^{3+} substitution rates are lower than 0.20 and 0.10,
459 respectively. For higher values, a mixture consisting of a substituted monoclinic phase with
460 the layered-perovskite structure and cubic phases, with the pyrochlore structure ($\text{Eu}_2\text{Ti}_2\text{O}_7$ and
461 $\text{Er}_2\text{Ti}_2\text{O}_7$) were found. In addition, the morphological features of $\text{La}_{2-x-y}\text{Eu}_x\text{Er}_y\text{Ti}_2\text{O}_7$ also
462 depends on the substitution rate. For low substitutions, we have noticed the presence of
463 aggregates of uniform submicron sized particles and, when the rates increase, the grain-size
464 distribution becomes random. Concerning the luminescence properties, we note intense lines,

465 assigned to Eu^{3+} transitions, centered at 612.5 nm when the samples are excited at 310 nm.
466 However, when the materials are excited at 377 nm, we noticed the presence of green
467 emission bands at 525 and 548 nm which correspond to transitions of Er^{3+} ions. Moreover, we
468 noticed the decrease of the average lifetime with the increase of Eu^{3+} ion content, which is
469 explained by a resonant energy transfer between Eu^{3+} and Er^{3+} ions. The CIE 1931
470 chromaticity coordinates were plotted versus the Eu^{3+} (and Er^{3+}) ions concentration. A shift
471 from red to orange was observed with the increase of Er^{3+} concentration and a shift from
472 orange to red was observed with the increase of Eu^{3+} concentration. The materials were also
473 dispersed in a glass matrix yielding brightly luminescent glass under the UV radiation. The
474 decrease of glass transparency due to phosphor incorporation was negligible. The
475 upconversion luminescence properties were checked by using two laser lines at 808 and 980
476 nm. For the later, a two photon mechanism was demonstrated and the observed bands
477 correspond to the emission of Er^{3+} ions. The average upconversion life times are 61.6 and
478 32.3 μs for 980 and 808 nm laser excitation, respectively. The evolution of the upconversion
479 luminescence with the temperature was investigated and it follows a Mott-Seitz behavior. To
480 finish, these oxides having these double luminescence properties under UV and NIR
481 excitation, can have several potential applications: i) their good thermal resistance allows
482 them to be dispersed in a glass matrix in order to create anti-counterfeit bottles for the luxury
483 perfume industry. The dispersion carried out in this study on a borate glass confirms this
484 potential; ii) These oxides could also be used to design inks that can be used for official
485 documents, ticketing and banknotes (their activities under two distinct wavelengths will
486 strengthen the document security); iii) After a toxicological study, these oxides could also be
487 used for applications in biology in particular as materials for labeling or as support materials
488 for phototherapy to activate a drug under the NIR excitation and also be detectable with the
489 UV microscopy surface excitation; iv) as materials for coupled detection of NIR and UV

490 radiation on the same material or v) more recently, it has been shown that these oxides, in the
491 form of single crystals, have low extinction coefficients in the visible range [69], [70]. As
492 such, the luminescence properties can be used for the design of laser crystals.

493

494

495 Acknowledgments

496 The work was financially supported by « les Ministères de l'Europe et des Affaires
497 Etrangères (MEAE) et de l'Enseignement Supérieur, de la Recherche et de l'Innovation
498 (MESRI) » and by the Ministry of Education and Science and the National Research Council
499 of Lithuania (PHC Gilibert (N° 373027ZC)). Chevreul Institute (FR 2638)", "Région Nord
500 Pas-de-Calais", "FEDER" and "C'Nano Nord-Ouest competence centre" are also
501 acknowledged for supporting and funding this work. The authors also thank Nora Djelal for
502 SEM analyses.

503

504 References

505

- 506 [1] A.H. Kitai, Principles of Luminescence, in: Lumin. Mater. Appl., John Wiley & Sons,
507 Ltd, 2008: pp. 1–18. <https://doi.org/10.1002/9780470985687.ch1>.
- 508 [2] A. Edgar, Luminescent Materials, in: S. Kasap, P. Capper (Eds.), Springer Handb.
509 Electron. Photonic Mater., Springer International Publishing, Cham, 2017: pp. 1–1.
510 https://doi.org/10.1007/978-3-319-48933-9_38.
- 511 [3] G. Blasse, B.C. Grabmaier, Luminescent Materials, Springer-Verlag, Berlin Heidelberg,
512 1994. ISBN 978-3-642-79017-1.
- 513 [4] Y.-C. Lin, M. Karlsson, M. Bettinelli, Inorganic Phosphor Materials for Lighting, Top.
514 Curr. Chem. 374 (2016) 21. <https://doi.org/10.1007/s41061-016-0023-5>.
- 515 [5] B. Lee, M. Kim, H.J. Kim, Y.B. Song, W.J. Yoo, S.H. Shin, D.E. Lee, K.W. Jang,
516 Measurement of Gamma-Rays Induced Luminescence Generated in a Sapphire Based
517 Fiber-Optic Radiation Sensor, J. Appl. Math. Phys. 4 (2016) 720–726.
518 <https://doi.org/10.4236/jamp.2016.48158>.
- 519 [6] X. Wang, O.S. Wolfbeis, R.J. Meier, Luminescent probes and sensors for temperature,
520 Chem. Soc. Rev. 42 (2013) 7834–7869. <https://doi.org/10.1039/C3CS60102A>.
- 521 [7] A. Mills, Phosphors development for LED lighting, III-Vs Rev. 18 (2005) 32–34.
522 [https://doi.org/10.1016/S0961-1290\(05\)01052-5](https://doi.org/10.1016/S0961-1290(05)01052-5).
- 523 [8] P. Kumar, S. Singh, B.K. Gupta, Future prospects of luminescent nanomaterial based
524 security inks: from synthesis to anti-counterfeiting applications, Nanoscale. 8 (2016)
525 14297–14340. <https://doi.org/10.1039/C5NR06965C>.
- 526 [9] H. Zhong, Z. Wang, W. Lu, J. Liu, Y. Wang, Luminescent Materials for 3D Display
527 Technology, in: R.-S. Liu (Ed.), Phosphors Convers. Nano Part. Quantum Dots Their

- 528 Appl., Springer Singapore, 2016: pp. 503–523. [https://doi.org/10.1007/978-981-10-1590-](https://doi.org/10.1007/978-981-10-1590-8_18)
529 [8_18](https://doi.org/10.1007/978-981-10-1590-8_18).
- 530 [10] F. Wang, D. Banerjee, Y. Liu, X. Chen, X. Liu, Upconversion nanoparticles in
531 biological labeling, imaging, and therapy, *The Analyst*. 135 (2010) 1839–1854.
532 <https://doi.org/10.1039/c0an00144a>.
- 533 [11] C. Feldmann, T. Jüstel, C.R. Ronda, P.J. Schmidt, *Inorganic Luminescent Materials:*
534 *100 Years of Research and Application*, *Adv. Funct. Mater.* 13 (2003) 511–516.
535 <https://doi.org/10.1002/adfm.200301005>.
- 536 [12] A. Gulzar, J. Xu, P. Yang, F. He, L. Xu, Upconversion processes: versatile biological
537 applications and biosafety, *Nanoscale*. 9 (2017) 12248–12282.
538 <https://doi.org/10.1039/C7NR01836C>.
- 539 [13] S. Chen, X. Liu, T. McHugh, Near-infrared deep brain stimulation via upconversion
540 nanoparticle-mediated optogenetics, in: *Opt. Biopsy XVII Real-Time Spectrosc.*
541 *Imaging Diagn.*, International Society for Optics and Photonics, 2019: p. 108730W.
542 <https://doi.org/10.1117/12.2506055>.
- 543 [14] H. Qiu, M. Tan, T.Y. Ohulchansky, J.F. Lovell, G. Chen, Recent Progress in
544 Upconversion Photodynamic Therapy, *Nanomaterials*. 8 (2018) 344.
545 <https://doi.org/10.3390/nano8050344>.
- 546 [15] Y. Yang, J. Mu, B. Xing, Photoactivated drug delivery and bioimaging, *Wiley*
547 *Interdiscip. Rev. Nanomed. Nanobiotechnol.* 9 (2017) e1408.
548 <https://doi.org/10.1002/wnan.1408>.
- 549 [16] A. Bayart, A. Katelnikovas, J.-F. Blach, J. Rousseau, S. Saitzek, Synthesis, structural
550 and luminescence properties of $(La_{1-x}Ln_x)_2Ti_2O_7$ (Ln=lanthanides) solid solutions, *J.*
551 *Alloys Compd.* 683 (2016) 634–646. <https://doi.org/10.1016/j.jallcom.2016.05.041>.
- 552 [17] A. Bayart, F. Szczepanski, J.F. Blach, J. Rousseau, A. Katelnikovas, S. Saitzek,
553 Upconversion luminescence properties and thermal quenching mechanisms in the
554 layered perovskite $La_{1.9}Er_{0.1}Ti_2O_7$ towards an application as optical temperature sensor,
555 *J. Alloys Compd.* (2018). <https://doi.org/10.1016/j.jallcom.2018.02.055>.
- 556 [18] S. Tabanlı, M. Erdem, B. Canturk, A. Mergen, G. Eryurek, Solid State Synthesis,
557 Structural and Up-Conversion Properties of Yb^{3+}/Er^{3+} and $Yb^{3+}/Tm^{3+}/Er^{3+}$ Doped
558 $La_2Ti_2O_7$ Phosphors, in: B. Di Bartolo, L. Silvestri, M. Cesaria, J. Collins (Eds.),
559 *Quantum Nano-Photonics*, Springer Netherlands, Dordrecht, 2018: pp. 449–451.
560 https://doi.org/10.1007/978-94-024-1544-5_54.
- 561 [19] H. Zhang, G. Li, Y. Zhu, S. Liu, K. Li, Y. Liang, Color tuning and white light emission
562 in a single-phased $La_2Ti_2O_7:Pr^{3+}, Tb^{3+}$ phosphor, *J. Alloys Compd.* 798 (2019) 800–
563 809. <https://doi.org/10.1016/j.jallcom.2019.05.306>.
- 564 [20] H. Yan, H. Ning, Y. Kan, P. Wang, M.J. Reece, Piezoelectric Ceramics with
565 Super-High Curie Points, *J. Am. Ceram. Soc.* 92 (2009) 2270–2275.
566 <https://doi.org/10.1111/j.1551-2916.2009.03209.x>.
- 567 [21] S. Nanamatsu, M. Kimura, K. Doi, S. Matsushita, N. Yamada, A new ferroelectric:
568 $La_2Ti_2O_7$, *Ferroelectrics*. 8 (1974) 511–513.
569 <https://doi.org/10.1080/00150197408234143>.
- 570 [22] H. Song, T. Peng, P. Cai, H. Yi, C. Yan, Hydrothermal synthesis of flaky crystallized
571 $La_2Ti_2O_7$ for producing hydrogen from photocatalytic water splitting, *Catal. Lett.* 113
572 (2007) 54–58. <https://doi.org/10.1007/s10562-006-9004-6>.
- 573 [23] K. Onozuka, Y. Kawakami, H. Imai, T. Yokoi, T. Tatsumi, J.N. Kondo, Perovskite-type
574 $La_2Ti_2O_7$ mesoporous photocatalyst, *J. Solid State Chem.* 192 (2012) 87–92.
575 <https://doi.org/10.1016/j.jssc.2012.03.055>.

- 576 [24] W.-M. Hou, Y. Ku, Synthesis and characterization of $\text{La}_2\text{Ti}_2\text{O}_7$ employed for
577 photocatalytic degradation of reactive red 22 dyestuff in aqueous solution, *J. Alloys*
578 *Compd.* 509 (2011) 5913–5918. <https://doi.org/10.1016/j.jallcom.2011.03.042>.
- 579 [25] D.W. Hwang, K.Y. Cha, J. Kim, H.G. Kim, S.W. Bae, J.S. Lee, Photocatalytic
580 Degradation of CH_3Cl over a Nickel-Loaded Layered Perovskite, *Ind. Eng. Chem. Res.*
581 42 (2003) 1184–1189. <https://doi.org/10.1021/ie020457c>.
- 582 [26] X. Li, H. Cai, L. Ding, X. Dou, W. Zhang, Synthesis and luminescence properties of
583 $\text{La}_2\text{Ti}_2\text{O}_7:\text{Er}^{3+}$ nanocrystals with pyrochlore structure, *J. Alloys Compd.* 541 (2012) 36–
584 40. <https://doi.org/10.1016/j.jallcom.2012.07.017>.
- 585 [27] M. Li, X.Y. Su, Y.M. Yang, L. Liu, F. Yu, X. Li, B. Han, J. Wu, H.J. Seo, Synthesis
586 and Photoluminescence Properties of $\text{La}_2\text{Ti}_2\text{O}_7:\text{Pr}^{3+}/\text{Tb}^{3+}$ Phosphors, *Sci. Adv. Mat.* 9
587 (2017) 587. <https://doi.org/info:doi/10.1166/sam.2017.2346>.
- 588 [28] Z. Shao, S. Saitzek, J.-F. Blach, A. Sayede, P. Roussel, R. Desfeux, Structural
589 Characterization and Photoluminescent Properties of $(\text{La}_{1-x}\text{Sm}_x)_2\text{Ti}_2\text{O}_7$ Solid Solutions
590 Synthesized by a Sol–Gel Route, *Eur. J. Inorg. Chem.* 2011 (2011) 3569–3576.
591 <https://doi.org/10.1002/ejic.201100309>.
- 592 [29] P.T. Diallo, P. Boutinaud, R. Mahiou, Anti-Stokes luminescence and site selectivity in
593 $\text{La}_2\text{Ti}_2\text{O}_7:\text{Pr}^{3+}$, *J. Alloys Compd.* 341 (2002) 139–143. [https://doi.org/10.1016/S0925-8388\(02\)00098-1](https://doi.org/10.1016/S0925-8388(02)00098-1).
- 595 [30] R.D. Shannon, Revised effective ionic radii and systematic studies of interatomic
596 distances in halides and chalcogenides, *Acta Crystallogr. Sect. A.* 32 (1976) 751–767.
597 <https://doi.org/10.1107/S0567739476001551>.
- 598 [31] Z. Shao, S. Saitzek, P. Roussel, O. Mentré, F. Prihor Gheorghiu, L. Mitoseriu, R.
599 Desfeux, Structural and dielectric/ferroelectric properties of $(\text{La}_{1-x}\text{Nd}_x)_2\text{Ti}_2\text{O}_7$
600 synthesized by sol–gel route, *J. Solid State Chem.* 183 (2010) 1652–1662.
601 <https://doi.org/10.1016/j.jssc.2010.05.004>.
- 602 [32] A.V. Prasadarao, U. Selvaraj, S. Komarneni, A.S. Bhalla, Sol-gel synthesis of $\text{Ln}_2(\text{Ln} =$
603 $\text{La}, \text{Nd})\text{Ti}_2\text{O}_7$, *J. Mater. Res.* 7 (1992) 2859–2863.
604 <https://doi.org/10.1557/JMR.1992.2859>.
- 605 [33] V.V. Atuchin, T.A. Gavrilova, J.-C. Grivel, V.G. Kesler, Electronic structure of layered
606 ferroelectric high- k titanate $\text{La}_2\text{Ti}_2\text{O}_7$, *J. Phys. Appl. Phys.* 42 (2009) 035305.
607 <https://doi.org/10.1088/0022-3727/42/3/035305>.
- 608 [34] D.S. Todorovsky, R.V. Todorovska, M.M. Milanova, D.G. Kovacheva, Deposition and
609 characterization of $\text{La}_2\text{Ti}_2\text{O}_7$ thin films via spray pyrolysis process, *Appl. Surf. Sci.* 253
610 (2007) 4560–4565. <https://doi.org/10.1016/j.apsusc.2006.10.016>.
- 611 [35] M. Suresh, A.V. Prasadarao, S. Komarneni, Mixed Hydroxide Precursors for $\text{La}_2\text{Ti}_2\text{O}_7$
612 and $\text{Nd}_2\text{Ti}_2\text{O}_7$ by Homogeneous Precipitation, *J. Electroceramics.* 6 (2001) 147–151.
613 <https://doi.org/10.1023/A:1011464902626>.
- 614 [36] P.A. Fuierer, R.E. Newnham, $\text{La}_2\text{Ti}_2\text{O}_7$ Ceramics, *J. Am. Ceram. Soc.* 74 (1991) 2876–
615 2881. <https://doi.org/10.1111/j.1151-2916.1991.tb06857.x>.
- 616 [37] Z. Shao, S. Saitzek, P. Roussel, R. Desfeux, Stability limit of the layered-perovskite
617 structure in $\text{Ln}_2\text{Ti}_2\text{O}_7$ ($\text{Ln} =$ lanthanide) thin films grown on (110)-oriented SrTiO_3
618 substrates by the sol–gel route, *J. Mater. Chem.* 22 (2012) 24894–24901.
619 <https://doi.org/10.1039/C2JM34729F>.
- 620 [38] S. Saitzek, Z. Shao, A. Bayart, P. Roussel, R. Desfeux, Microstructure and Nanoscale
621 Piezoelectric/Ferroelectric Properties in $\text{Ln}_2\text{Ti}_2\text{O}_7$ ($\text{Ln} =$ Lanthanide) Thin Films with
622 Layered Perovskite Structure, in: P. Granger, V.I. Parvulescu, V.I. Parvulescu, W.
623 Prellier (Eds.), *Perovskites Relat. Mix. Oxides*, Wiley-VCH Verlag GmbH & Co.
624 KGaA, 2016: pp. 233–258.

- 625 <http://onlinelibrary.wiley.com/doi/10.1002/9783527686605.ch11/summary> (accessed
626 January 6, 2017).
- 627 [39] M. Gasperin, Ditanate de lanthane, *Acta Crystallogr. B.* 31 (1975) 2129–2130.
628 <https://doi.org/10.1107/S0567740875007005>.
- 629 [40] E.H. Chtoun, L. Hanebali, P. Garnier, Analyse par diffraction des rayons x, méthode de
630 rietveld, de la structure des solutions solides $(1-x)\text{A}_2\text{Ti}_2\text{O}_7 - x\text{Fe}_2\text{TiO}_5$ A= Eu, Y, *Ann.*
631 *Chim. Sci. Matér.* 26 (2001) 27–32.
- 632 [41] G.C. Lau, B.D. Muegge, T.M. McQueen, E.L. Duncan, R.J. Cava, Stuffed rare earth
633 pyrochlore solid solutions, *J. Solid State Chem.* 179 (2006) 3126–3135.
634 <https://doi.org/10.1016/j.jssc.2006.06.007>.
- 635 [42] J. Tauc, Optical properties and electronic structure of amorphous Ge and Si, *Mater. Res.*
636 *Bull.* 3 (1968) 37–46. [https://doi.org/10.1016/0025-5408\(68\)90023-8](https://doi.org/10.1016/0025-5408(68)90023-8).
- 637 [43] F.X. Zhang, J. Lian, U. Becker, R.C. Ewing, L.M. Wang, J. Hu, S.K. Saxena, Structural
638 change of layered perovskite $\text{La}_2\text{Ti}_2\text{O}_7$ at high pressures, *J. Solid State Chem.* 180
639 (2007) 571–576. <https://doi.org/10.1016/j.jssc.2006.11.022>.
- 640 [44] B. Zhou, Z. Xiao, A. Huang, L. Yan, F. Zhu, J. Wang, P. Yin, H. Wang, Effect of Tm–
641 Er concentration ratio on the photoluminescence of Er–Tm: Al_2O_3 thin films fabricated
642 by pulsed laser deposition, *Prog. Nat. Sci.* 18 (2008) 661–664.
643 <https://doi.org/10.1016/j.pnsc.2008.01.009>.
- 644 [45] P.S. Peijzel, A. Meijerink, R.T. Wegh, M.F. Reid, G.W. Burdick, A complete $4f\{sup n\}$
645 energy level diagram for all trivalent lanthanide ions, *J. Solid State Chem.* 178 (2005).
646 <https://doi.org/10.1016/j.jssc.2004.07.046>.
- 647 [46] T. Pussacq, H. Kabbour, S. Colis, H. Vezin, S. Saitzek, O. Gardoll, C. Tassel, H.
648 Kageyama, C. Laberty Robert, O. Mentré, Reduction of $\text{Ln}_2\text{Ti}_2\text{O}_7$ Layered Perovskites:
649 A Survey of the Anionic Lattice, Electronic Features, and Potentials, *Chem. Mater.* 29
650 (2017) 1047–1057. <https://doi.org/10.1021/acs.chemmater.6b03808>.
- 651 [47] G.H. Dieke, H.M. Crosswhite, H. Crosswhite, Spectra and energy levels of rare earth
652 ions in crystals, Interscience Publishers, New York, 1968.
- 653 [48] N. Ben Amar, T. Koubaa, M.A. Hassairi, I. Kbaïli, M. Dammak, Optical spectroscopy
654 of Eu^{3+} ions doped in $\text{YAl}_3(\text{BO}_3)_4$ crystal, *J. Lumin.* 160 (2015) 95–100.
655 <https://doi.org/10.1016/j.jlumin.2014.11.045>.
- 656 [49] Z. Sun, Q. Zhang, Y. Li, H. Wang, Thermal stable $\text{La}_2\text{Ti}_2\text{O}_7:\text{Eu}^{3+}$ phosphors for blue-
657 chip white LEDs with high color rendering index, *J. Alloys Compd.* 1 (2010) 338–342.
658 <https://doi.org/10.1016/j.jallcom.2010.06.203>.
- 659 [50] V.V. Atuchin, A.S. Aleksandrovsky, O.D. Chimitova, T.A. Gavrilova, A.S. Krylov,
660 M.S. Molocheev, A.S. Oreshonkov, B.G. Bazarov, J.G. Bazarova, Synthesis and
661 Spectroscopic Properties of Monoclinic $\alpha\text{-Eu}_2(\text{MoO}_4)_3$, *J. Phys. Chem. C.* 118 (2014)
662 15404–15411. <https://doi.org/10.1021/jp5040739>.
- 663 [51] J. Rocha, L.D. Carlos, J.P. Rainho, Z. Lin, P. Ferreira, R.M. Almeida,
664 Photoluminescence of new Er^{3+} -doped titanosilicate materials, *J. Mater. Chem.* 10
665 (2000) 1371–1375. <https://doi.org/10.1039/A910192F>.
- 666 [52] J. Zhang, X. Wang, W.-T. Zheng, X.-G. Kong, Y.-J. Sun, X. Wang, Structure and
667 luminescence properties of $\text{TiO}_2:\text{Er}^{3+}$ nanocrystals annealed at different temperatures,
668 *Mater. Lett.* 61 (2007) 1658–1661. <https://doi.org/10.1016/j.matlet.2006.07.093>.
- 669 [53] G. Blasse, Energy transfer in oxidic phosphors, *Phys. Lett. A.* 28 (1968) 444–445.
670 [https://doi.org/10.1016/0375-9601\(68\)90486-6](https://doi.org/10.1016/0375-9601(68)90486-6).
- 671 [54] H. Liu, L. Liao, Z. Xia, Structure, luminescence property and energy transfer behavior
672 of color-adjustable $\text{La}_5\text{Si}_2\text{BO}_{13}:\text{Ce}^{3+},\text{Mn}^{2+}$ phosphors, *RSC Adv.* 4 (2014) 7288–7295.
673 <https://doi.org/10.1039/C3RA47223J>.

- 674 [55] J.R. Lakowicz, Principles of Fluorescence Spectroscopy, Springer Science & Business
675 Media, 2007. ISBN 978-0-387-46312-4.
- 676 [56] B. Pahari, S. Chakraborty, B. Sengupta, S. Chaudhuri, W. Martin, J. Taylor, J. Henley,
677 D. Davis, P.K. Biswas, A.K. Sharma, P.K. Sengupta, Biophysical Characterization of
678 Genistein in Its Natural Carrier Human Hemoglobin Using Spectroscopic and
679 Computational Approaches, Food and Nutrition Sciences 4 (2013) 83-92.
680 <https://doi.org/10.4236/fns.2013.48A011>.
- 681 [57] F. Könz, Y. Sun, C.W. Thiel, R.L. Cone, R.W. Equall, R.L. Hutcheson, R.M.
682 Macfarlane, Temperature and concentration dependence of optical dephasing, spectral-
683 hole lifetime, and anisotropic absorption in $\text{Eu}^{3+}:\text{Y}_2\text{SiO}_5$, Phys. Rev. B. 68 (2003)
684 085109. <https://doi.org/10.1103/PhysRevB.68.085109>.
- 685 [58] G.E. Khalil, K. Lau, G.D. Phelan, B. Carlson, M. Gouterman, J.B. Callis, L.R. Dalton,
686 Europium beta-diketonate temperature sensors: Effects of ligands, matrix, and
687 concentration, Rev. Sci. Instrum. 75 (2004) 192–206.
688 <https://doi.org/10.1063/1.1632997>.
- 689 [59] K. Maheshvaran, K. Marimuthu, Concentration dependent Eu^{3+} doped boro-tellurite
690 glasses—Structural and optical investigations, J. Lumin. 9 (2012) 2259–2267.
691 <https://doi.org/10.1016/j.jlumin.2012.04.022>.
- 692 [60] N. Bloembergen, Solid State Infrared Quantum Counters, Phys. Rev. Lett. 2 (1959) 84–
693 85. <https://doi.org/10.1103/PhysRevLett.2.84>.
- 694 [61] F. Auzel, Compteur quantique par transfert d'énergie entre deux ions de terres rares
695 dans un tungstate mixte et dans un verre, C. R. Acad. Sci. Paris 262 (1966) 1016–1019.
- 696 [62] M. Pollnau, D.R. Gamelin, S.R. Lüthi, H.U. Güdel, M.P. Hehlen, Power dependence of
697 upconversion luminescence in lanthanide and transition-metal-ion systems, Phys. Rev.
698 B. 61 (2000) 3337–3346. <https://doi.org/10.1103/PhysRevB.61.3337>.
- 699 [63] X. Cai, J.E. Martin, L.E. Shea-Rohwer, K. Gong, D.F. Kelley, Thermal Quenching
700 Mechanisms in II–VI Semiconductor Nanocrystals, J. Phys. Chem. C. 117 (2013) 7902–
701 7913. <https://doi.org/10.1021/jp400688g>.
- 702 [64] D.W. Cooke, B.L. Bennett, R.E. Muenchausen, J.-K. Lee, M.A. Nastasi, Intrinsic
703 ultraviolet luminescence from Lu_2O_3 , Lu_2SiO_5 and $\text{Lu}_2\text{SiO}_5:\text{Ce}^{3+}$, J. Lumin. 106 (2004)
704 125–132. <https://doi.org/10.1016/j.jlumin.2003.09.001>.
- 705 [65] Theoretical Basis of Luminescence Phenomena, in: Therm. Opt. Stimul. Lumin., John
706 Wiley & Sons, Ltd, 2011: pp. 7–28. <https://doi.org/10.1002/9781119993766.ch2>.
- 707 [66] F. Sidirolou, S. A. Wade, N. M. Dragomir, G. W. Baxter, S. F. Collins, Effects of
708 high-temperature heat treatment on Nd^{3+} -doped optical fibers for use in fluorescence
709 intensity ratio based temperature sensing. Rev. Sci. Instrum. 74, (2003) 3524–3530.
710 <https://doi.org/10.1063/1.1578706>.
- 711 [67] X. Wang, X. Kong, Y. Yu, Y. Sun, H. Zhang, Effect of Annealing on Upconversion
712 Luminescence of $\text{ZnO}:\text{Er}^{3+}$ Nanocrystals and High Thermal Sensitivity. J. Phys. Chem.
713 C 111, (2007) 15119–15124. <https://doi.org/10.1021/jp0686689>.
- 714 [68] X. Li, Effects of Er^{3+} concentration on down-/up-conversion luminescence and
715 temperature sensing properties in $\text{NaGdTiO}_4:\text{Er}^{3+}/\text{Yb}^{3+}$ phosphors. Ceram. Int. 42,
716 (2016) 14710–14715. <https://doi.org/10.1016/j.ceramint.2016.06.096>.
- 717 [69] Z. Wang, G. Zhou, D. Jiang, S. Wang, Recent development of $\text{A}_2\text{B}_2\text{O}_7$ system
718 transparent ceramics, J. Adv. Ceram. 7 (2018) 289–306. <https://doi.org/10.1007/s40145-018-0287-z>.
- 720 [70] A. Bayart, J.-F. Blach, M. Huvé, F. Blanchard, P. Roussel, R. Desfeux, S. Saitzek,
721 Optical properties of $\text{Ln}_2\text{Ti}_2\text{O}_7$ (with Ln = La to Lu) thin films grown on (110)- SrTiO_3
722 substrates by pulsed laser deposition, Opt. Mater. 92 (2019) 303–310.
723 <https://doi.org/10.1016/j.optmat.2019.04.049>.

724

725 **Figure captions**

726

727 **Figure 1.** XRD patterns of $\text{La}_{2-x-y}\text{Eu}_x\text{Er}_y\text{Ti}_2\text{O}_7$. The stars indicate the cubic/pyrochlore phases.

728

729 **Figure 2.** SEM images of (a) $\text{La}_{1.94}\text{Eu}_{0.05}\text{Er}_{0.01}\text{Ti}_2\text{O}_7$, (b) $\text{La}_{1.90}\text{Eu}_{0.05}\text{Er}_{0.05}\text{Ti}_2\text{O}_7$, (c)
730 $\text{La}_{1.60}\text{Eu}_{0.10}\text{Er}_{0.30}\text{Ti}_2\text{O}_7$, (d) $\text{La}_{1.55}\text{Eu}_{0.40}\text{Er}_{0.05}\text{Ti}_2\text{O}_7$.

731

732 **Figure 3.** Diffuse reflectance UV-Visible spectra and Tauc plots for $\text{La}_{1.85}\text{Eu}_{0.10}\text{Er}_{0.05}\text{Ti}_2\text{O}_7$,
733 $\text{Er}_2\text{Ti}_2\text{O}_7$ and $\text{Eu}_2\text{Ti}_2\text{O}_7$ oxides.

734

735 **Figure 4.** Luminescence properties of $\text{La}_{1.6}\text{Eu}_{0.10}\text{Er}_{0.30}\text{Ti}_2\text{O}_7$ oxide: (a) Room-temperature
736 excitation spectra recorded in the range of 250 to 575 nm at $\lambda_{\text{em}}=547.5$ nm and $\lambda_{\text{em}}=612.5$ nm;
737 (b) Room-temperature emission spectra recorded in the range of 450 to 800 nm at $\lambda_{\text{exc}}=310$
738 nm and $\lambda_{\text{exc}}=377$ nm.

739

740 **Figure 5.** a) Photographs highlighting emission color of $\text{La}_{2-x-y}\text{Eu}_x\text{Er}_y\text{Ti}_2\text{O}_7$ oxides under
741 excitation at 365 nm; b) Intensity evolution of $^5\text{S}_{3/2} \rightarrow ^4\text{I}_{15/2}$ transition vs. y in $\text{La}_{1.90-}$
742 $y\text{Eu}_{0.10}\text{Er}_y\text{Ti}_2\text{O}_7$ oxides under $\lambda_{\text{exc}}=310, 377$ and 393 nm ; c) Intensities evolutions of $^5\text{D}_0 \rightarrow$
743 $^7\text{F}_4$ and $^5\text{D}_0 \rightarrow ^7\text{F}_2$ transitions vs. x in $\text{La}_{1.95-x}\text{Eu}_x\text{Er}_{0.05}\text{Ti}_2\text{O}_7$ oxides under $\lambda_{\text{exc}}=310$ and 377
744 393 nm ; d) Intensities evolutions of $^5\text{D}_0 \rightarrow ^7\text{F}_4$ and $^5\text{D}_0 \rightarrow ^7\text{F}_2$ transitions vs. y in in $\text{La}_{1.90-}$
745 $y\text{Eu}_{0.10}\text{Er}_y\text{Ti}_2\text{O}_7$ oxides under $\lambda_{\text{exc}}=310$ and 377 nm.

746

747 **Figure 6.** a) Photoluminescence decay curves of $\text{La}_{1.95-x}\text{Eu}_x\text{Er}_{0.05}\text{Ti}_2\text{O}_7$ oxides b) Evolution of
748 the average lifetime as a function of the x value under an excitation of 393 nm.

749

750 **Figure 7.** a) 3D plot and b) 2D projection of CIE 1931 coordinates of $\text{La}_{1.95-x}\text{Eu}_x\text{Er}_{0.05}\text{Ti}_2\text{O}_7$
751 oxides; c) 3D plot and d) 2D projection of CIE 1931 coordinates of $\text{La}_{1.90-y}\text{Eu}_{0.10}\text{Er}_y\text{Ti}_2\text{O}_7$.

752

753 **Figure 8.** Transmittance spectra of glass alone and glass loaded with 2% by weight of
754 $\text{La}_{1.60}\text{Eu}_{0.30}\text{Er}_{0.10}\text{Ti}_2\text{O}_7$ oxide (inset, photograph of the glass wafer under natural light and
755 under UV excitation).

756

757 **Figure 9.** a) Photographs highlighting the emission color variation of $\text{La}_{2-x-y}\text{Eu}_x\text{Er}_y\text{Ti}_2\text{O}_7$
758 oxides under 785 nm laser excitation (40 mW) b) Upconversion emission spectra of
759 $\text{La}_{1.85}\text{Eu}_{0.10}\text{Er}_{0.05}\text{Ti}_2\text{O}_7$ with two exciting laser (808 and 980 nm); c) Upconversion emission
760 spectra of $\text{La}_{1.85}\text{Eu}_{0.10}\text{Er}_{0.05}\text{Ti}_2\text{O}_7$ ($\lambda_{\text{ex}}=980$ nm) at different laser power (from 0.05 W to 0.98
761 W) recorded at room temperature; d) Power dependence of upconversion luminescence from
762 $^4\text{S}_{3/2} \rightarrow ^4\text{I}_{15/2}$ and $^4\text{F}_{9/2} \rightarrow ^4\text{I}_{15/2}$ transitions.

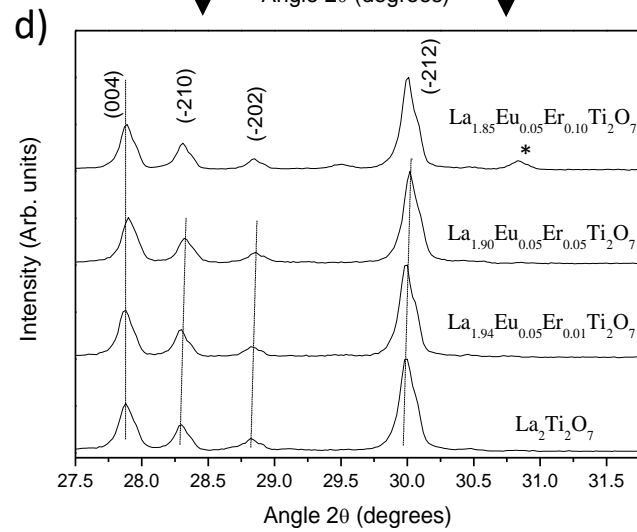
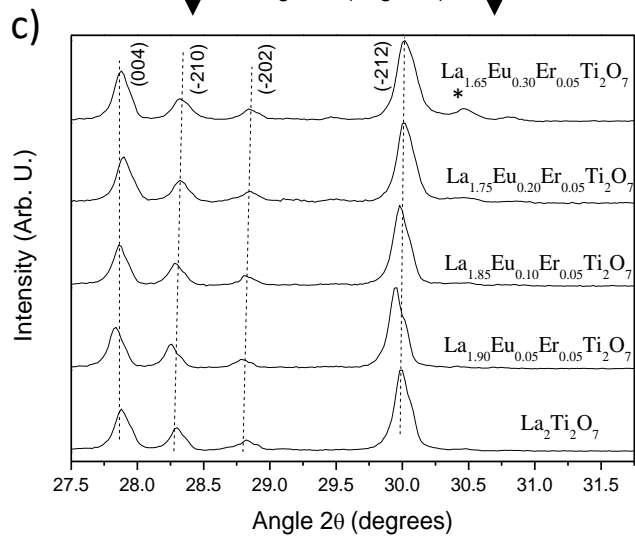
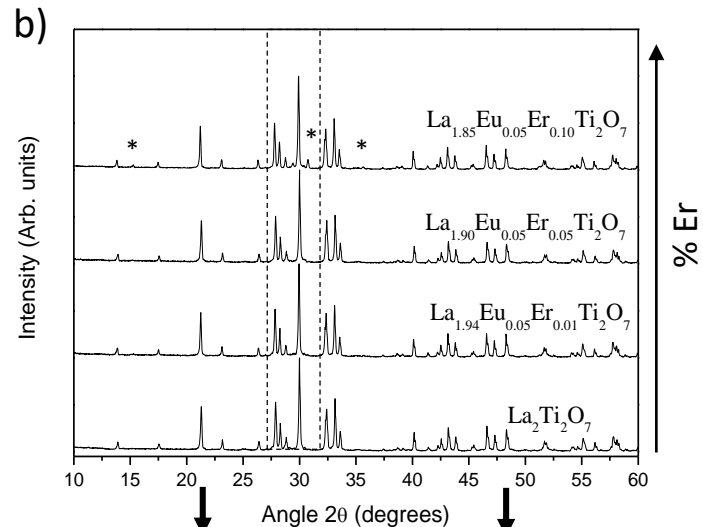
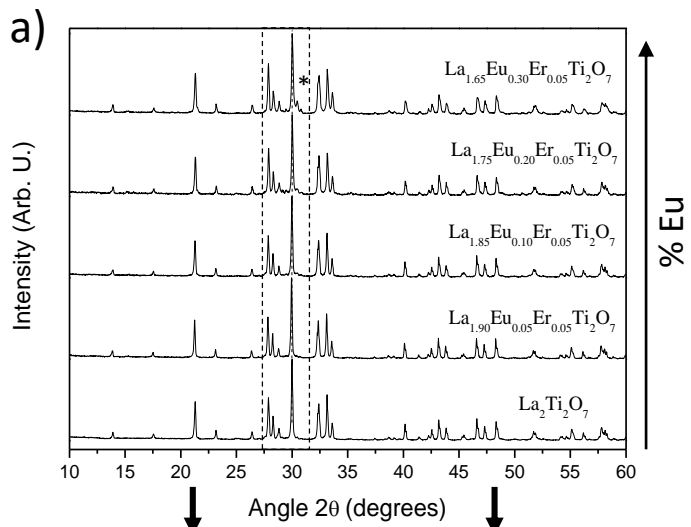
763

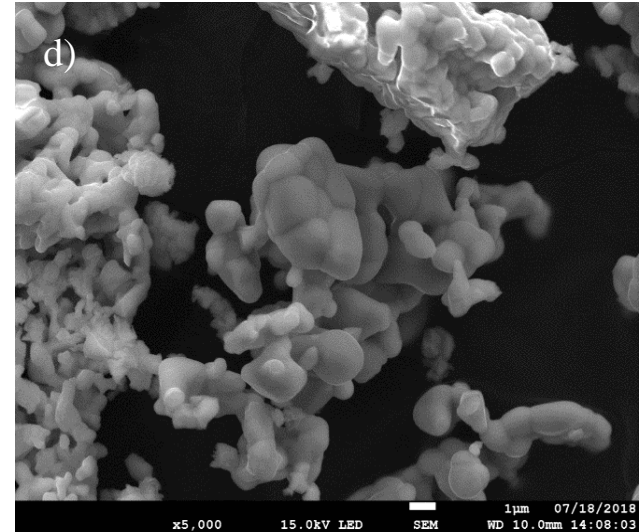
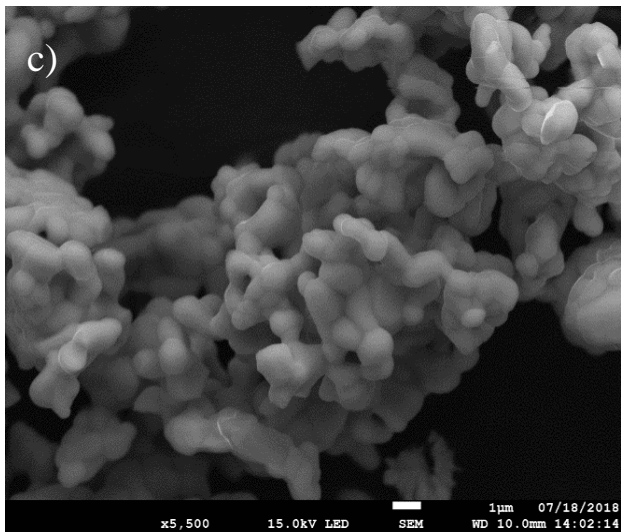
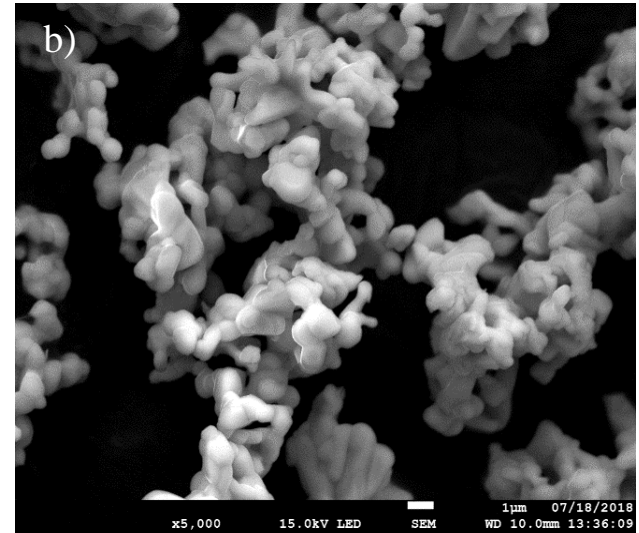
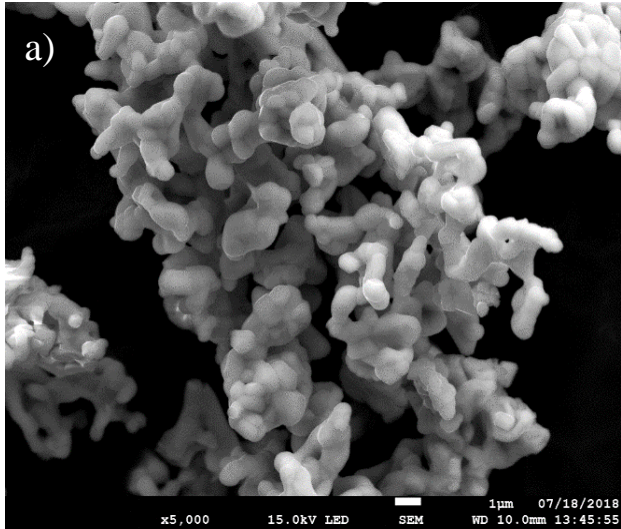
764 **Figure 10.** Upconversion decays curves performed for $^4\text{F}_{9/2} \rightarrow ^4\text{I}_{15/2}$ transition and obtained
765 under 808 and 980 nm laser excitation. The blue curve represents the Instrument Response
766 Function (IRF) for a laser pulse at 808 nm.

767

768 **Figure 11.** a) Emission spectra ($\lambda_{\text{ex}}=980$ nm) vs. temperature of $\text{La}_{1.85}\text{Eu}_{0.10}\text{Er}_{0.05}\text{Ti}_2\text{O}_7$ oxide
769 in a range of 77 to 500 K; b) Evolution of UC intensity as a function of the temperature for
770 $^4\text{F}_{9/2} \rightarrow ^4\text{I}_{15/2}$ transition (inset a plot of $\ln(I_0/I-1)$ as a function of $1/T$ for the determination of
771 the activation energy).

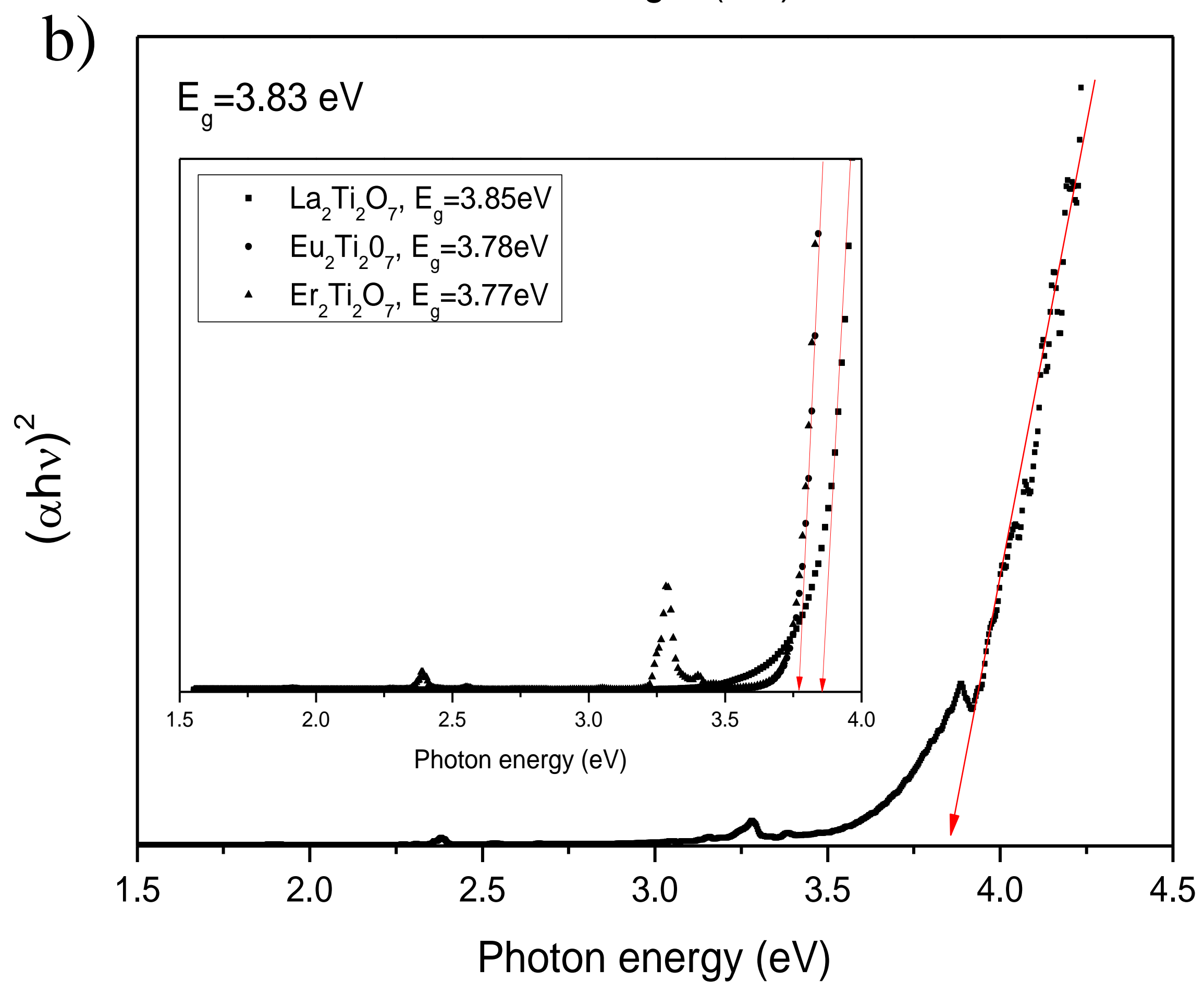
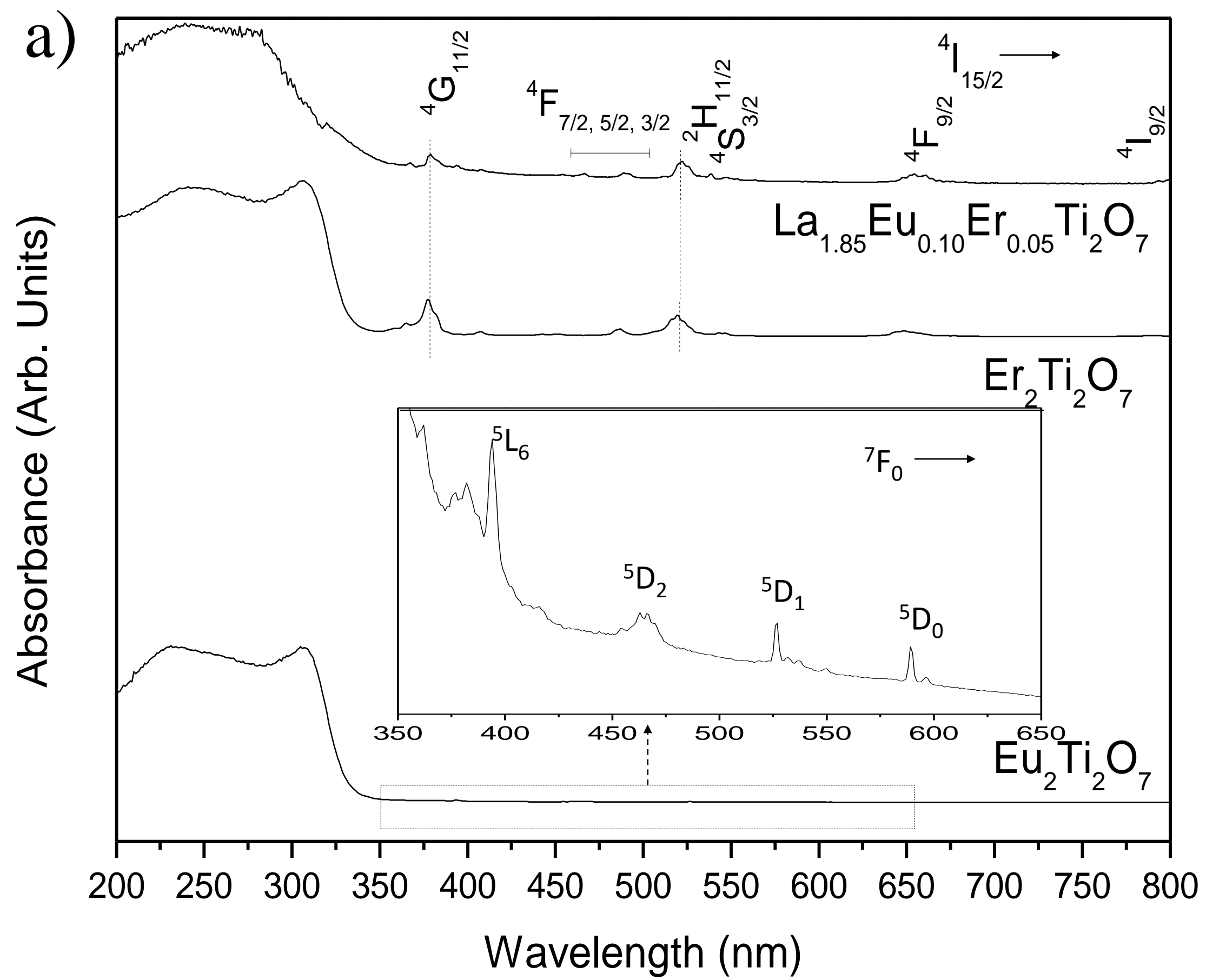
772





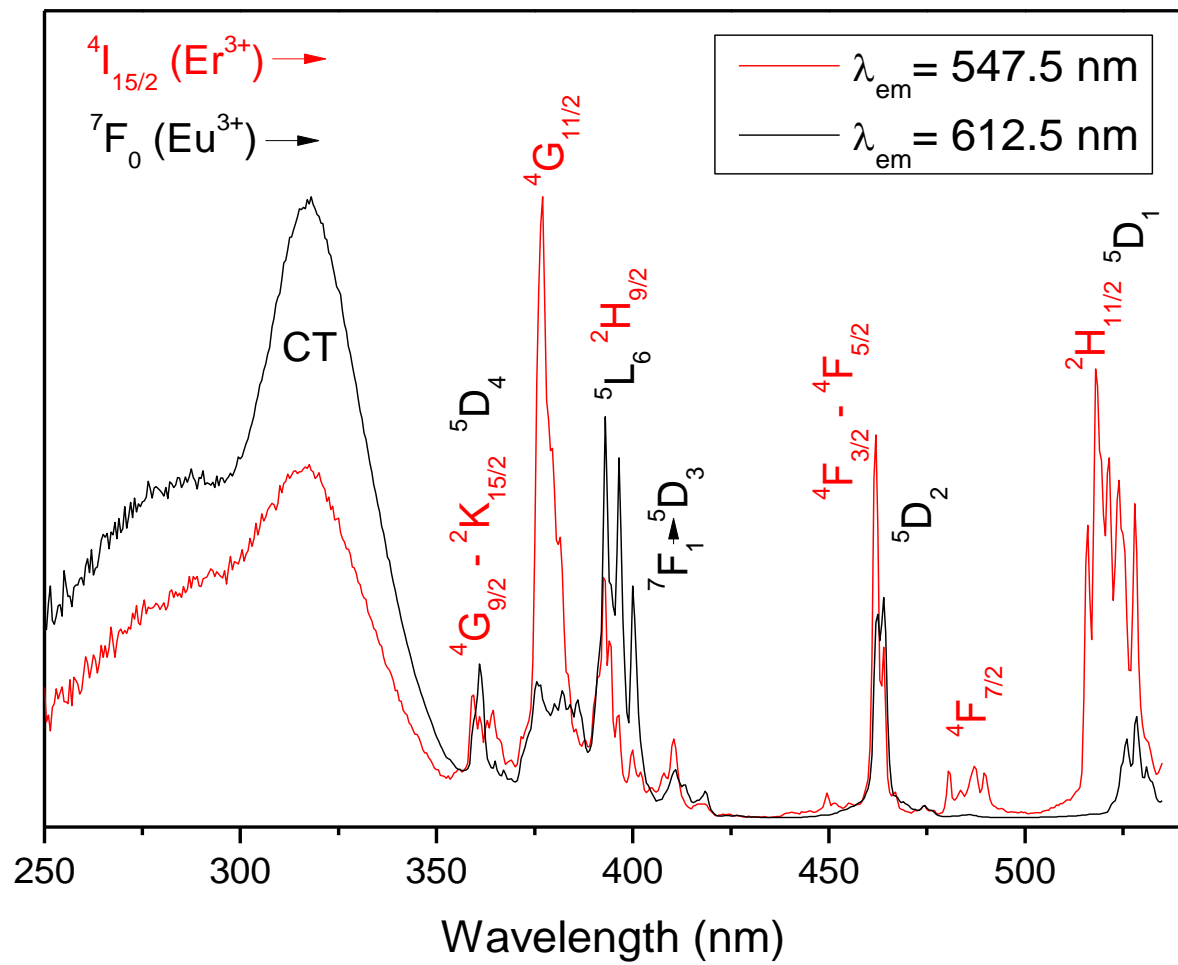
% Er

% Eu



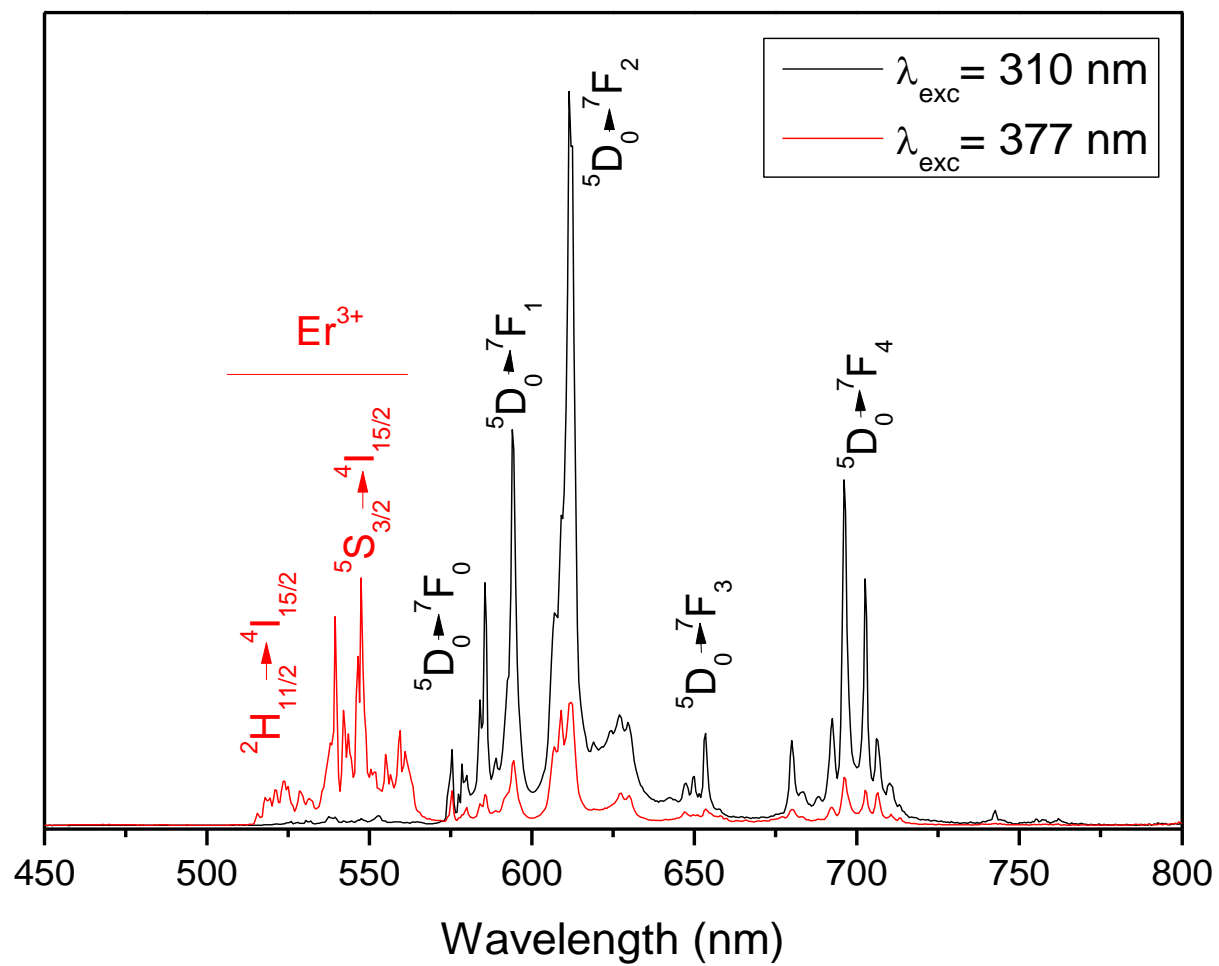
a)

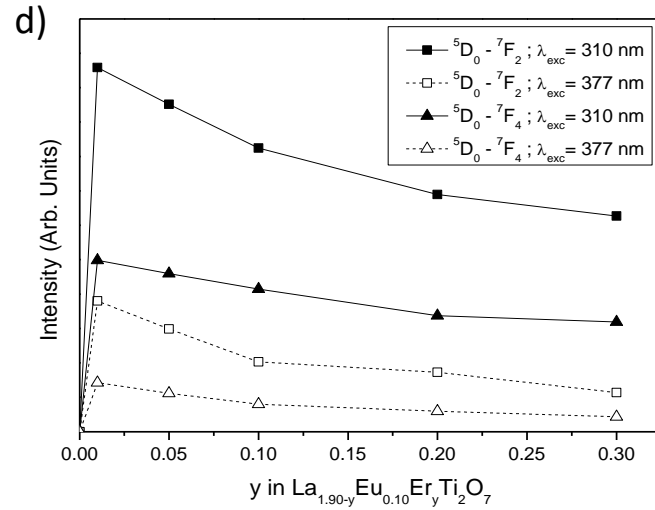
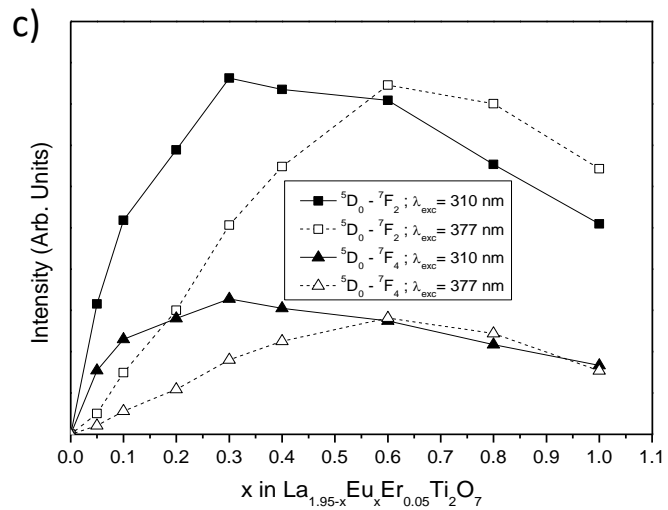
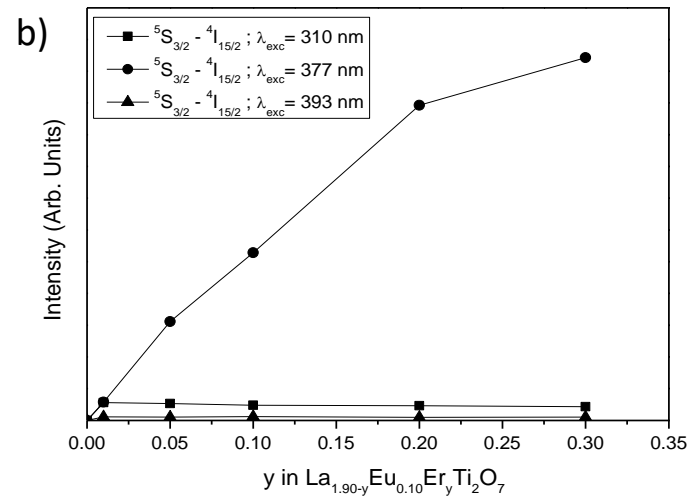
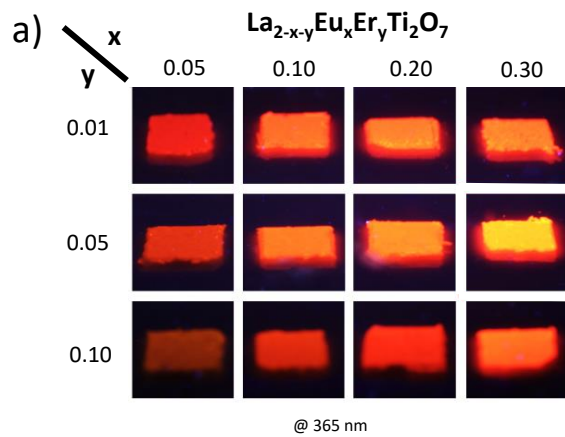
Normalized Intensity (Arb. Units)

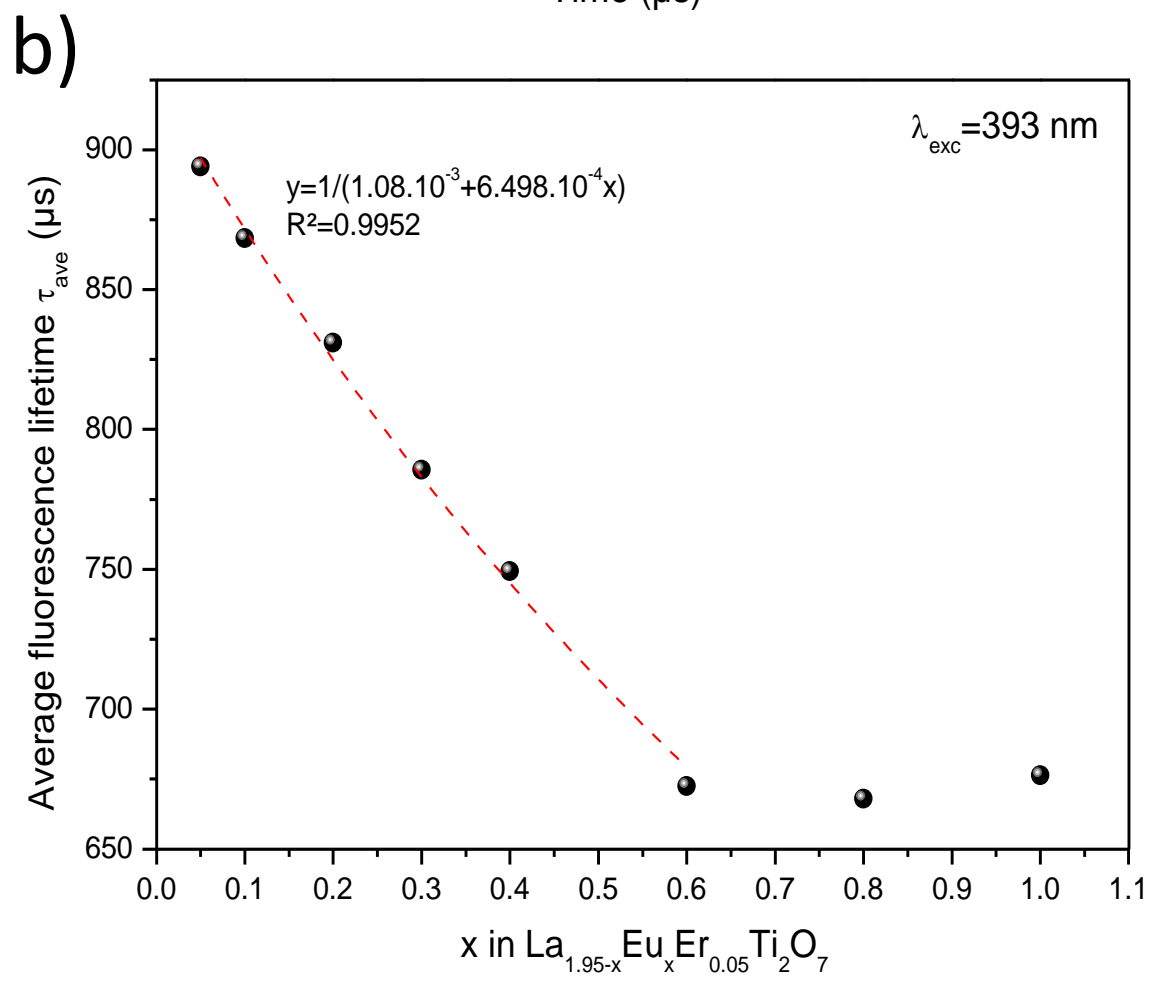
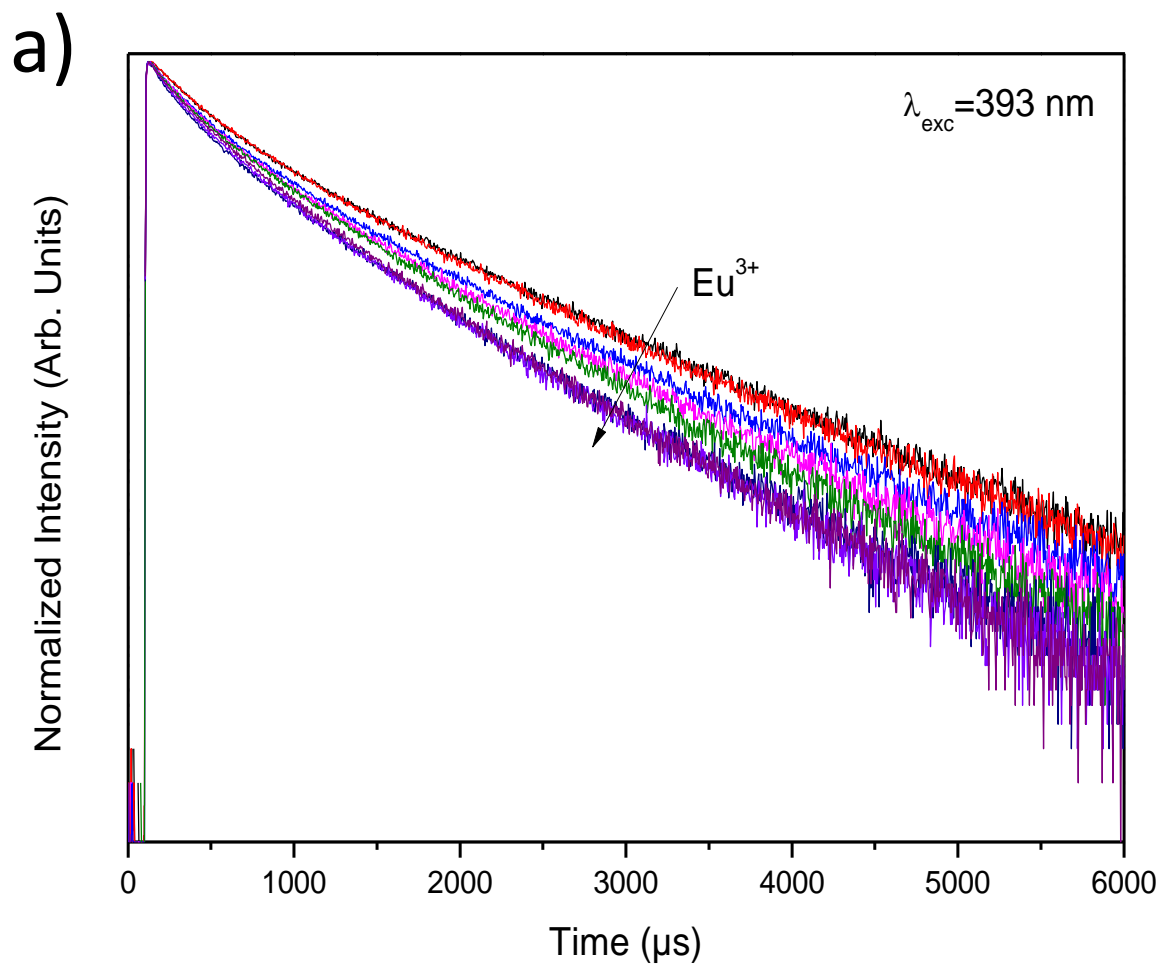


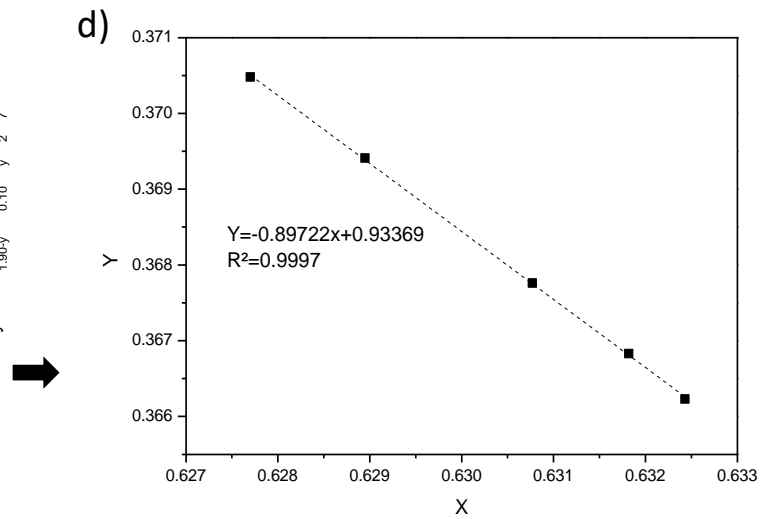
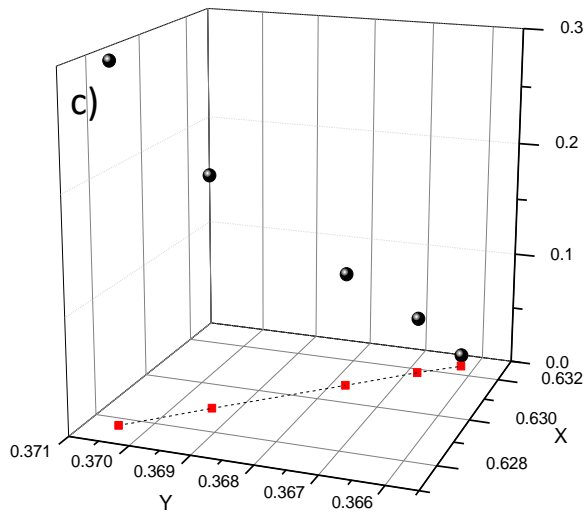
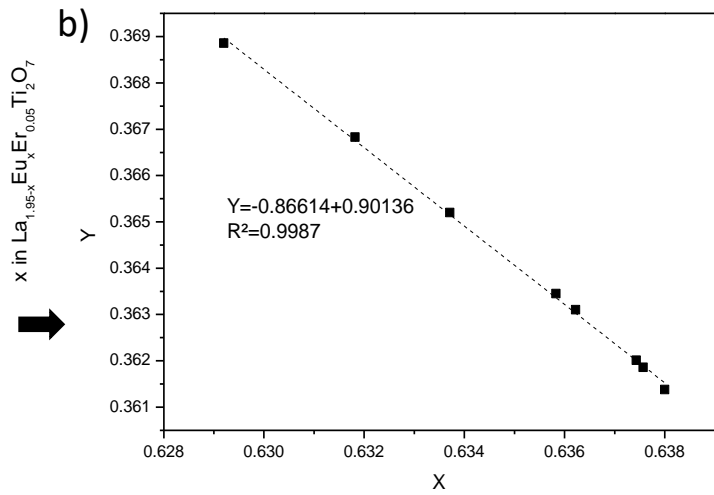
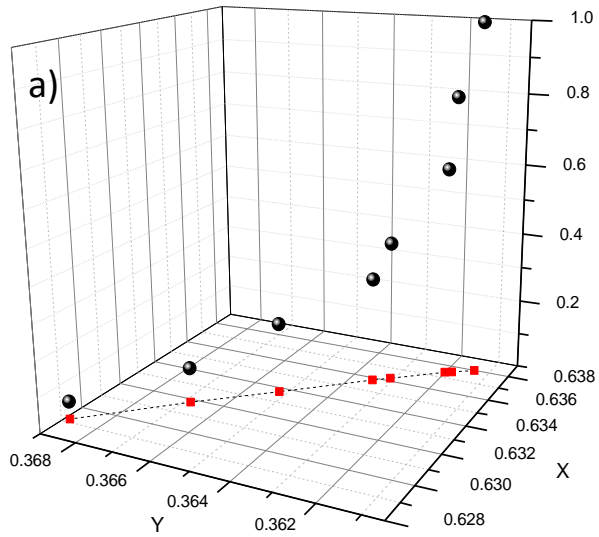
b)

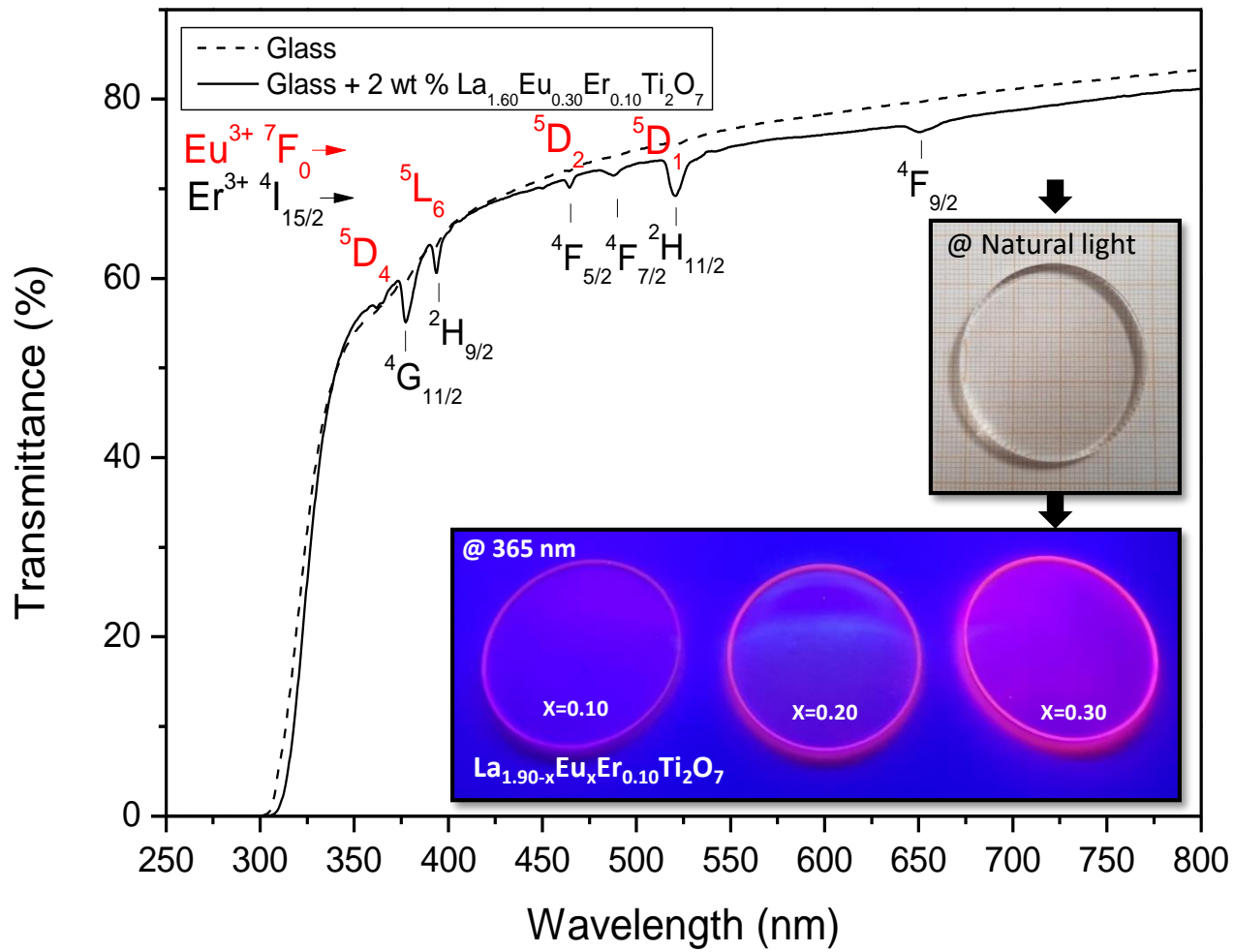
Normalized Intensity (Arb. Units)

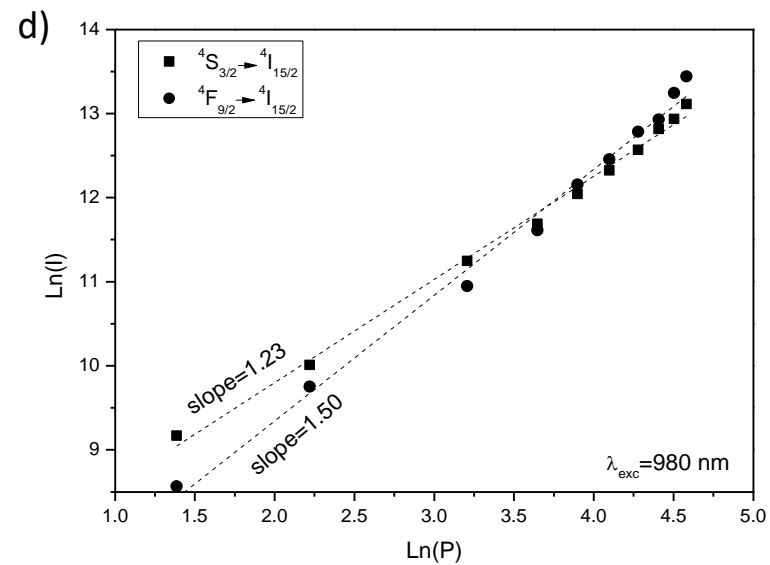
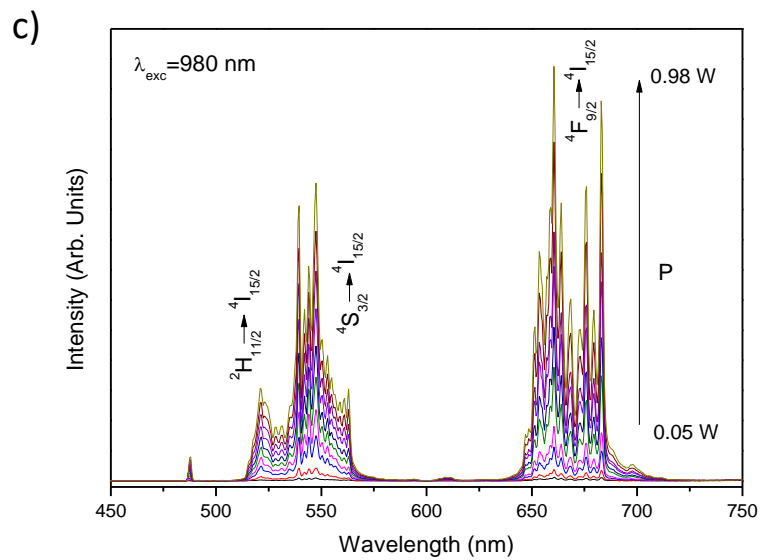
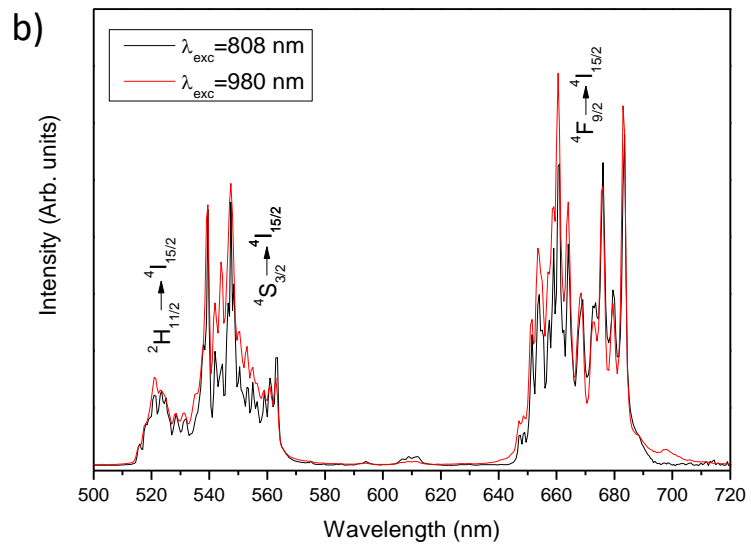
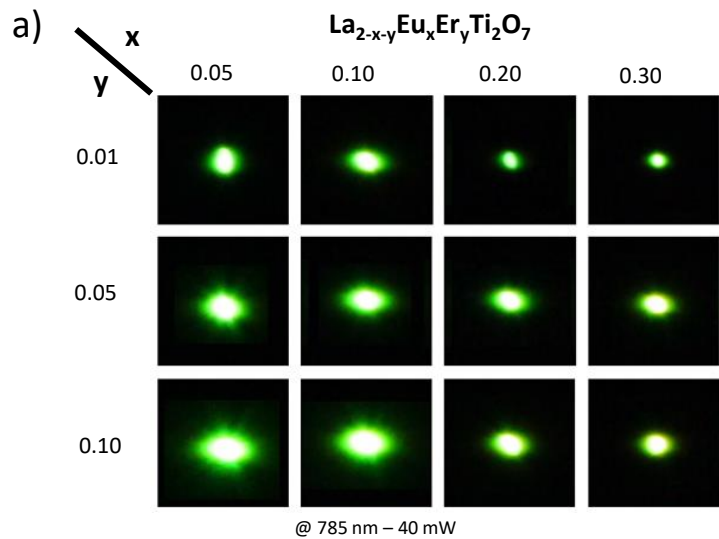


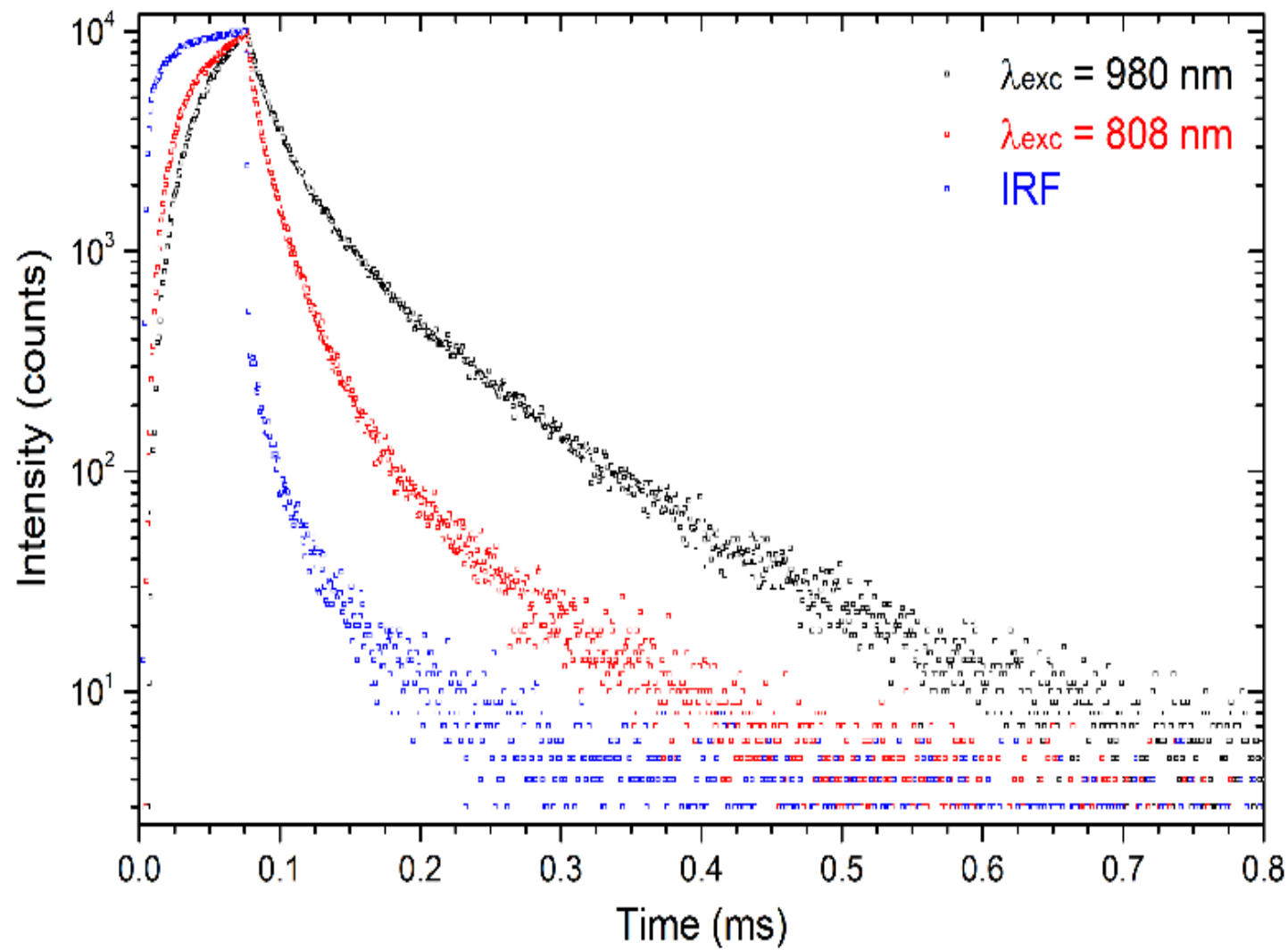


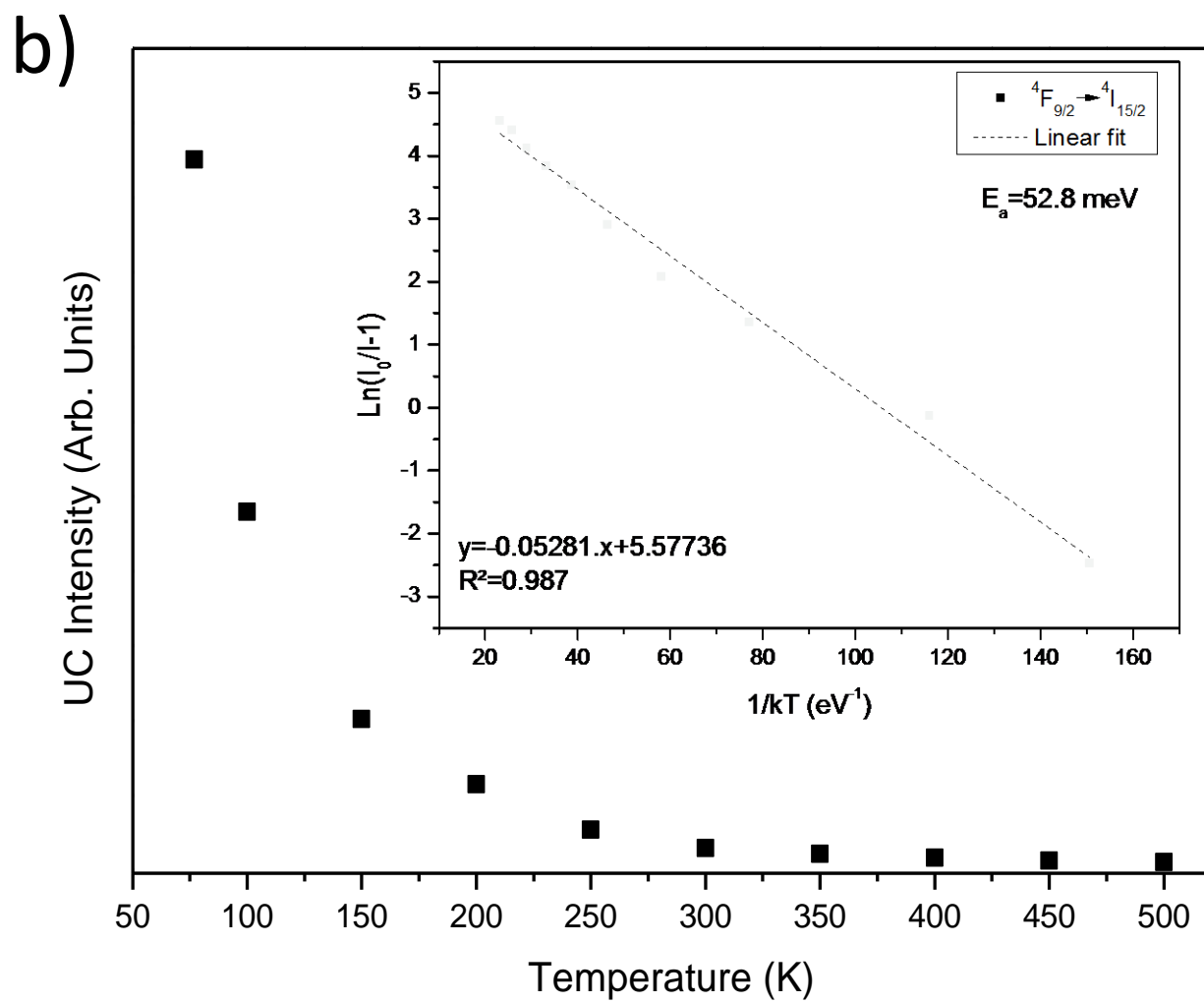
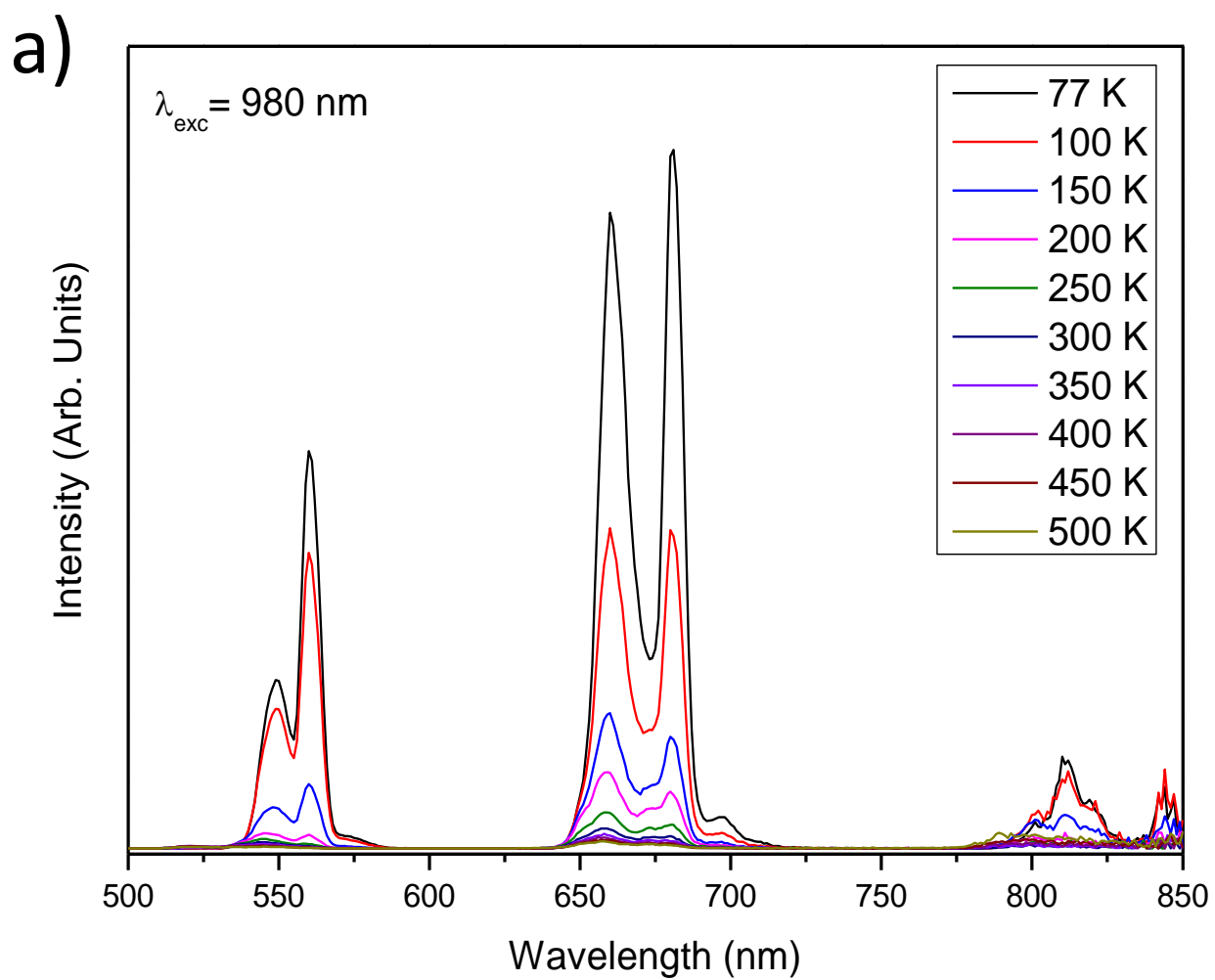


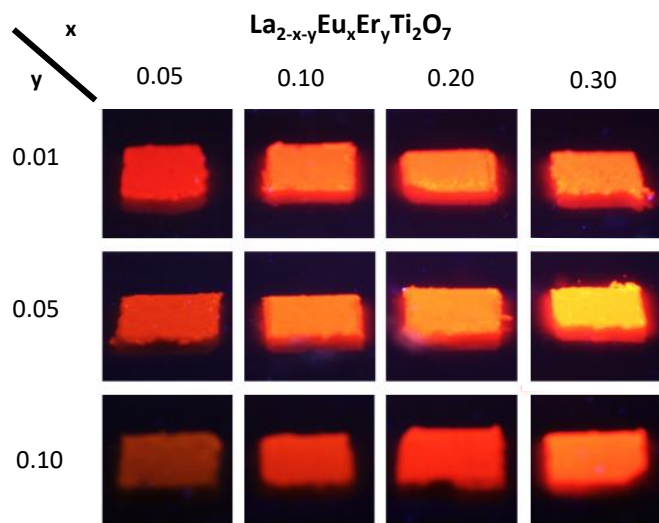




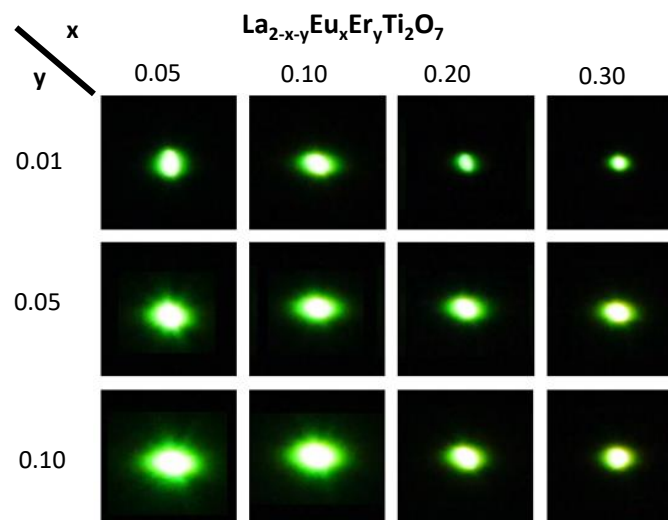








@ 365 nm



@ 785 nm – 40 mW

